

# Integral field spectroscopy of nearby QSOs: I. ENLR size – luminosity relation, ongoing star formation & resolved gas-phase metallicities <sup>\*</sup>

B. Husemann<sup>1,2,†</sup>, K. Jahnke,<sup>3</sup> S. F. Sánchez<sup>4,5,6</sup>, L. Wisotzki<sup>2</sup>,  
D. Nugroho<sup>3</sup>, D. Kupko<sup>2</sup>, M. Schramm<sup>7</sup>

<sup>1</sup>European Southern Observatory, Karl-Schwarzschild-Str. 2, 85748 Garching b. München, Germany

<sup>2</sup>Leibniz-Institut für Astrophysik Potsdam, An der Sternwarte 16, 14482 Potsdam, Germany

<sup>3</sup>Max-Planck-Institut für Astronomie, Königstuhl 17, D-69117 Heidelberg, Germany

<sup>4</sup>Instituto de Astronomía, Universidad Nacional Autónoma de México, A.P. 70-264, 04510, México, D.F.

<sup>5</sup>Instituto de Astrofísica de Andalucía (IAA/CSIC), Glorieta de la Astronomía s/n Aptdo. 3004, E-18080 Granada, Spain

<sup>6</sup>Centro Astronómico Hispano-Alemán, Calar Alto (CSIC-MPG), C/Jesús Durbán Remón 2-2, E-04004 Almería, Spain

<sup>7</sup>Kavli Institute for the Physics and Mathematics of the Universe (WPI), Todai Institutes for Advanced Study, the University of Tokyo, Kashiwa, Japan 277-8583

18 June 2014

## ABSTRACT

We present optical integral field spectroscopy for a flux-limited sample of 19 quasi-stellar objects (QSOs) at low redshift ( $z < 0.2$ ) and spatially resolve their ionized gas properties at a physical resolution of 2–5 kpc. Extended ionized gas exists in all QSO host galaxies irrespective of their morphological types. The extended narrow-line regions (ENLRs), photoionized by the radiation of active galactic nuclei (AGN), have sizes of up to several kpc and correlate more strongly with the QSO continuum luminosity at 5100 Å than with the integrated [OIII] luminosity. We find a relation of the form  $\log r \propto (0.46 \pm 0.04) \log L_{5100}$ , reinforcing the picture of an approximately constant ionization parameter for the ionized clouds across the ENLR. Besides the ENLR, we also find gas ionized by young massive stars in more than 50 per cent of the galaxies on kpc scales. In more than half of the sample, the specific star formation rates based on the extinction-corrected H $\alpha$  luminosity are consistent with those of inactive disc-dominated galaxies, even for some bulge-dominated QSO hosts. Enhanced star formation rates of up to  $\sim 70 M_{\odot} \text{ yr}^{-1}$  are rare and always associated with signatures of major mergers. Comparison with the star formation rate based on the 60  $\mu\text{m}$  + 100  $\mu\text{m}$  FIR luminosity suggests that the FIR luminosity is systematically contaminated by AGN emission and H $\alpha$  appears to be a more robust and sensitive tracer for the star formation rate. Evidence for efficient AGN feedback is scarce in our sample, but some of our QSO hosts lack signatures of ongoing star formation leading to a reduced specific star formation rate with respect to the main sequence of galaxies. Whether this is causally linked to the AGN or simply caused by gas depletion remains an open question. Based on 12 QSOs where we can make measurements, we find that on average bulge-dominated QSO host galaxies tend to fall below the mass-metallicity relation compared to their disc-dominated counterparts. While not yet statistically significant for our small sample, this may provide a useful diagnostic for future large surveys if this metal dilution can be shown to be linked to recent or ongoing galaxy interactions.

**Key words:** Galaxies: active - quasars: emission-lines - Galaxies: ISM - Galaxies: evolution - Galaxies: star formation - ISM: abundances

## 1 INTRODUCTION

Active galactic nuclei (AGN) are powered by gas accretion on to super-massive black holes at the centre of galaxies and have been thought to significantly affect the evolution of their host galaxies through quenching of star formation in the most massive systems. Very luminous AGN, recognized as quasi-stellar objects (QSOs), were often found in major mergers, which have been thought to be

<sup>\*</sup> Based on observations made with VIMOS integral field spectrograph mounted to the Melipal VLT telescope at ESO-Paranal Observatory (programs 072B-0550 and 083B-0801; PI: K. Jahnke)

<sup>†</sup> ESO fellow, bhuseman@eso.org

the main triggering mechanism for a QSO phase. This has led to an evolutionary scenario for the formation of bulge-dominated galaxies from gas-rich major merger with enhanced star formation that is followed by a QSO phase to quench star formation (e.g. Sanders et al. 1988a,b; Hutchings & Neff 1992; Canalizo & Stockton 2001; Hopkins et al. 2006) and resulting in the passive spheroidal galaxies we observe at present. However, the AGN-merger connection is strongly debated and an unsolved issue. On one hand, several studies found an increased fraction of AGN in galaxies with close companions, ongoing mergers or in post-merger systems (Koss et al. 2010; Ramos Almeida et al. 2010; Ellison et al. 2011; Bessiere et al. 2012; Cotini et al. 2013; Sabater, Best & Argudo-Fernández 2013). On the other hand, many studies claimed to find no significant excess of mergers in AGN hosts (Dunlop et al. 2003; Sánchez et al. 2004b; Grogin et al. 2005; Li et al. 2008; Gabor et al. 2009; Tal et al. 2009; Cisternas et al. 2011; Kocevski et al. 2012; Schawinski et al. 2012; Böhm et al. 2013). These studies report that a significant fraction of AGN appear to reside in isolated disc-dominated galaxies for which internal processes are likely responsible for fuelling their active nuclei. Both findings could be in agreement when the AGN-merger connection is a function of AGN luminosity as reported by Treister et al. (2012), considering the large number of disturbed host galaxies for the most luminous QSOs in the local Universe (e.g. Veilleux et al. 2009). On the other hand, the morphological analysis of X-ray selected AGN host galaxies at  $0.5 < z < 0.8$  indicate no significant luminosity dependence of the AGN-merger connection (Villforth et al. 2014). A potential problem in the interpretation of the current data is that the faint signatures of recent interactions can easily be missed when the image depth is too shallow (e.g. Bennert et al. 2008) or that there could be a significant time delay between the onset of AGN activity and the merger event (e.g. Wild, Heckman & Charlot 2010).

The exceptionally blue colours of bulge-dominated QSO host galaxies compared to their passive inactive counterparts (e.g. Kauffmann et al. 2003; Jahnke et al. 2004a,b; Sánchez et al. 2004b; Zakamska et al. 2006; Schramm, Wisotzki & Jahnke 2008) imply the presence of a significant population of young stars. These QSO hosts were therefore thought to be in a transition phase during which continued star formation is suppressed as a consequence of AGN feedback supporting the merger-induced evolution. The presence of an intermediate-age stellar population (1-2Gyr) has been subsequently confirmed with deep long-slit spectroscopy (Canalizo & Stockton 2001; Jahnke et al. 2007; Wold et al. 2010; Canalizo & Stockton 2013). However, it is observationally difficult to reliably quantify the amount of ongoing star formation in these luminous QSOs and results based on [OII] line strength from unresolved spectroscopy (Ho 2005; Silverman et al. 2009) and infrared diagnostics (e.g. Schweitzer et al. 2006; Lacy et al. 2007; Santini et al. 2012; Rosario et al. 2012; Urrutia et al. 2012) are strongly debated. Those studies lead to inconsistent results on the enhancement or suppression of ongoing star formation in AGN hosts.

One particular problem in estimating the ongoing star formation from optical line luminosities is the coupling between QSO radiation and the interstellar gas of the host galaxy. It is well established that AGN can ionize the gas out to several kpc, the so-called extended narrow-line region (ENLR), Unger et al. 1987, based on narrow-band imaging of the [OIII]  $\lambda 5007$  emission line (e.g. McCarthy et al. 1987; Stockton & MacKenty 1987; Bennert et al. 2002; Schmitt et al. 2003; Villar-Martín et al. 2010). Only spatially resolved quantitative spectroscopy is able to separate the relative contribution of HII regions powered by young massive stars and AGN photoionization across the host galaxies. A severe problem

for studying luminous type 1 (unobscured) QSO from the ground is the seeing that smears out the light of the bright nucleus. Thus, long-slit and integral field spectroscopic studies often focused on type 2 (obscured) QSOs to study the ENLR (e.g. Humphrey et al. 2010; Greene et al. 2011; Villar-Martín et al. 2011; Liu et al. 2013). The light of the nucleus is blocked by obscuring material along our line of sight (Antonucci 1993) which minimizes any host galaxy contamination for type 2 QSOs. However, the intrinsic properties of the AGN, like the accretion rate, black hole mass and AGN luminosity can only be indirectly estimated for those QSOs and are subject to systematic uncertainties.

In this article, we present rest-frame optical integral field spectroscopy observations of a flux-limited sample of 19 nearby ( $z < 0.2$ ) type 1 QSOs, which correspond to the most luminous AGN at their respective redshifts. We use a dedicated algorithm to decompose the QSO and host galaxy light in the three-dimensional data which we have already successfully applied to similar observations of QSOs (Sánchez et al. 2004a; Christensen et al. 2006; Husemann et al. 2008, 2010, 2011, 2013b). We leave a detailed analysis of the stellar populations as well as gas and stellar kinematics for future papers in the series and focus solely on the spatially resolved characterization of the ionized gas via standard emission-line diagnostics. Specifically, we separate HII-like regions and the ENLR contribution to study the ENLR size-luminosity relation for type 1 AGN and estimate specific star formation rates (SSFRs) from HII-like regions in comparison to the overall population of normal galaxies. Furthermore, we measure the gas-phase oxygen abundance as a diagnostic for the origin of the gas, which can be used to distinguish between internal processes and galaxy interactions as AGN triggering mechanisms in different morphological types.

In Section 2, we present the QSO sample, and describe the IFU observations and data reduction. In Section 3, we outline the QSO-host galaxy deblending process and provide a detailed description of the emission-line measurements together with the corresponding ionized gas diagnostics in Section 4. Our main results are presented and discussed in Section 5 followed by our summary and conclusions (Section 6). Throughout the paper we assume a cosmological model with  $H_0 = 70 \text{ km s}^{-1} \text{ Mpc}^{-1}$ ,  $\Omega_m = 0.3$ , and  $\Omega_\Lambda = 0.7$ .

## 2 QSO SAMPLE AND OBSERVATIONS

### 2.1 Sample characteristics

Our flux-limited QSO sample is drawn from the Hamburg/ESO survey (HES, Reimers, Koehler & Wisotzki 1996; Wisotzki et al. 1996, 2000) and consists of the brightest QSOs above well defined flux limits within an area of  $611 \text{ deg}^2$  at  $0.027 < z < 0.2$ . It is a low-redshift subset of the sample defined by Köhler et al. (1997) to study the local QSO luminosity function where details of the sample selection can be found. The QSOs have total apparent magnitudes in the range of  $13.7 < V_{\text{total}} < 16.8$ , and host magnitudes of  $14.5 < V_{\text{host}} < 18.0$  with corresponding host luminosities of  $-25.6 < M_K < -23.2$  in the  $K$  band. We summarize their main characteristics in Table 1 and describe them below in more detail.

An extensive set of ground-based multi-colour *BVRJHK* imaging observation for this sample is available and was presented by Jahnke, Kuhlbrodt & Wisotzki (2004). It contains 9 bulge-dominated QSO host galaxies, 8 disc-dominated QSO host galaxies, and 2 cases of ongoing major mergers. In addition, a few objects have confirmed close companion galaxies with or without signatures of ongoing interactions. High-resolution *HST* images were

**Table 1.** Overview of the sample characteristics

Object	$z$	$m_V^a$	Morph. <sup>b</sup>	$R_e^c$ [kpc]	$M_K^d$	$\log(M_*/M_\odot)^e$	$R^f$	$L_{1.4\text{ GHz}}^g$ [W/Hz]	$L_{60\mu\text{m}}^h$ [Jy]	$L_{100\mu\text{m}}^h$ [Jy]
HE 0952–1552	0.112	15.8	D	5.1	-25.5	$11.18 \pm 0.28$	3.4	23.23	<0.2	<1.0
HE 1019–1414	0.076	16.1	D	3.7	-24.1	$10.77 \pm 0.28$	2.6	22.86	<0.2	<1.0
HE 1020–1022 <sup>†</sup>	0.196	16.6	B	8.1	-25.8	$11.45 \pm 0.27$	779.7	25.95	<0.2	<1.0
HE 1029–1401 <sup>†</sup>	0.085	13.7	B	3.1	-25.8	$11.10 \pm 0.38$	0.6	23.43	<0.2	<1.0
HE 1043–1346 <sup>†</sup>	0.068	15.7	D	5.0	-24.9	$10.88 \pm 0.38$	< 2.5	< 22.16	0.36	1.51
HE 1110–1910 <sup>†</sup>	0.111	16.0	B	4.2	-24.8	$10.81 \pm 0.32$	< 1.0	< 22.60	<0.2	<1.0
HE 1201–2409	0.140	16.3	B	1.1	-25.3	$10.96 \pm 0.32$	< 1.6	< 22.81	<0.2	<1.0
HE 1228–1637 <sup>†</sup>	0.104	15.8	B	2.6	-24.6	$10.79 \pm 0.30$	< 0.7	< 22.54	<0.2	<1.0
HE 1237–2252	0.097	15.9	D	7.4	-25.4	$11.14 \pm 0.18$	< 1.6	< 22.48	<0.2	<1.0
HE 1239–2426 <sup>†</sup>	0.082	15.6	D	6.8	-25.2	$11.15 \pm 0.19$	1.9	22.60	0.37	1.12
HE 1254–0934	0.139	14.9	M	12.2	-25.2	$11.19 \pm 0.24$	2.0	23.89	0.92	1.09
HE 1300–1325	0.046	14.9	B	3.6	-24.8	$10.75 \pm 0.39$	< 0.6	< 21.81	0.47	1.24
HE 1310–1051 <sup>†</sup>	0.034	14.9	D	2.5	-23.2	$10.21 \pm 0.27$	< 0.3	< 21.55	<0.2	<1.0
HE 1315–1028	0.099	16.8	D	6.1	-24.2	$10.71 \pm 0.31$	< 2.0	< 22.49	<0.2	<1.0
HE 1335–0847	0.080	16.3	B	3.7	-23.9	$10.48 \pm 0.31$	< 1.9	< 22.30	<0.2	<1.0
HE 1338–1423	0.041	13.7	D	10.0	-25.4	$11.09 \pm 0.32$	0.5	22.29	<0.2	<1.0
HE 1405–1545	0.196	16.2	M	6.9	-25.6	$11.24 \pm 0.38$	< 0.9	< 23.12	<0.2	<1.0
HE 1416–1256 <sup>†</sup>	0.129	16.4	B	4.9	-24.5	$10.45 \pm 0.39$	5.9	22.95	<0.2	<1.0
HE 1434–1600 <sup>†</sup>	0.147	15.7	B	5.5	-25.7	$11.10 \pm 0.36$	417.5	25.71	<0.2	<1.0

<sup>a</sup>Total apparent  $V$  band magnitude. <sup>b</sup>Morphological classification of the QSO hosts: D – disc-dominated/late-type galaxies, B – bulge-dominated/early-type galaxies, and M – ongoing major mergers. <sup>c</sup>Effective (half-light) radius of the QSO hosts as reported by Jahnke, Kuhlbrodt & Wisotzki (2004) converted to our adopted cosmology. <sup>d</sup> $k$ -corrected absolute  $K$ -band magnitudes of the QSO hosts as reported by Jahnke, Kuhlbrodt & Wisotzki (2004). <sup>e</sup>Total stellar masses of the QSO hosts based on multi-color SED fits (Schramm et al. in prep.). <sup>f</sup> $R$  parameter defined as the flux density ratio at 6 cm over that at 4400Å. <sup>g</sup>Continuum radio luminosity at 1.4 GHz. <sup>h</sup>IRAS 60 $\mu\text{m}$  and 100 $\mu\text{m}$  fluxes and upper limits from the IRAS Faint Source Catalogue v2.0 (Moshir & et al. 1990). <sup>†</sup>Objects with available high resolution HST imaging data.

obtained for 9 objects in different programs<sup>1</sup>, some of which are unpublished so far. We retrieved all archival *HST* images from the Hubble Legacy Archive<sup>2</sup> and performed a deblending of the QSO and host components with GALFIT (Peng et al. 2002, 2010) using either a dedicated PSF star observation or, alternatively, a PSF model created with TINYTIM (Krist 1995). The QSO-subtracted *HST* or ground-based images (mainly  $V$ -band) of our targets are shown in the overview figures (Fig. 4) for each object later on.

We used the broad-band photometric information available in either 6 or 7 different bands to infer the stellar mass for each host galaxy by estimating their mass-to-light ratio via a SED template fitting approach. We generated a set of template SEDs with the Bruzual & Charlot (2003) population synthesis code assuming Padova 1994 evolutionary tracks and a Chabrier initial mass function (IMF). Furthermore, we adopted a solar metallicity for all template SEDs. Since our host galaxies exhibit bluer colours than the inactive ones (Jahnke, Kuhlbrodt & Wisotzki 2004), we account for signs of ongoing or recent star formation by creating a library of 2190 composite stellar population (CSP) models. The CSP models are two component models with exponential declining star formation histories. The e-folding times are chosen to be  $\tau = 10$  Myr and 100 Myr, respectively, for the recent burst components and  $\tau = 1$  Gyr for the old stellar population. Finally, we esti-

mate the stellar masses of each host galaxy using a template-fitting algorithm where the redshift of the templates is fixed to the known redshift of the QSO during the  $\chi^2$  minimization. To assess the uncertainty of our stellar mass estimates, we varied the observed flux in each bandpass according to the Gaussian distributed  $\sigma$  flux error. Here, we also included the effect of contamination from emission lines falling into the bandpass. After fitting 100 of those mock SEDs we defined the confidence interval such that it covers 99% of the range in stellar masses around the best fit value.

To characterize the radio properties of our sample, we classified the QSOs into radio-loud, radio-intermediate and radio-quiet based on the  $R$  parameter (e.g. Kellermann et al. 1989), which is defined as the ratio of the flux density at 6 cm (5 GHz) over that at 4400Å. Follow-up observations for HES QSOs at 5 GHz with the Very Large Array (VLA) were only done for 7 QSOs of our sample. For the other objects we used the measurements and upper limits from the NRAO VLA Sky Survey (NVSS) at 1.4 GHz (Condon et al. 1998) as a surrogate for the radio flux at 5 GHz assuming a power-law radio spectral index of  $\alpha_r = -0.5$  at the dividing line between steep and flat-spectrum radio source. The vast majority (12/19) of the QSOs in the sample are radio-quiet QSOs ( $R < 1$ ), including all objects with an upper limit in  $R$  close to 1. Five QSOs exhibit an intermediate level of radio emission with  $R$  parameters in between  $1 \leq R \leq 10$  and two QSOs in our sample ( $\sim 10$  per cent), HE 1020–1022 and HE 1434–1600, are clearly radio-loud QSOs ( $R > 10$ ).

In addition, we collected the IRAS 60 $\mu\text{m}$  and 100 $\mu\text{m}$  fluxes from the IRAS Faint Source Catalogue (Moshir & et al. 1990). Only four objects in our sample have been detected by IRAS. For the rest of the sample, we adopt upper limits of 0.2 Jy and 1.0 Jy,

<sup>1</sup> *HST* images from the following programs: “The nature of quasar host galaxies: combining ACS imaging and VLT Integral Field Spectroscopy” (Proposal 10238, PI: F. Courbin), “Subarcsecond structure in nearby AGN” (Proposal 5479, PI: M. Malkan), “WFC imaging of nearby bright Quasars” (Proposal 5434, PI: J. Bahcall), “High-resolution imaging of X-ray selected AGN” (Proposal 6361, PI: B. Boyle)

<sup>2</sup> Website of the Hubble Legacy Archive: <http://hla.stsci.edu>

respectively, which were estimated by Moshir & et al. (1990) for the catalogue.

## 2.2 VIMOS integral field spectroscopy

Integral field spectroscopy of all 19 QSOs in the sample was obtained with the VISIBLE MultiObject Spectrograph (VIMOS, Le Fèvre et al. 2003) mounted on UT3 (Melipal) of the ESO Very Large Telescope in Chile. The observations were carried out in service mode in period 72 and 83 during dark time. We used the high resolution grisms (HR grisms) in order to be able to obtain accurate kinematic information from emission and absorption lines as well as to detect and deblend kinematically different emission-line components. The spectral resolution of the HR blue, HR orange, and HR red grisms are  $\lambda \Delta\lambda^{-1} \sim 2550$ ,  $\sim 2650$  and  $\sim 3100$ , respectively. Because the wavelength coverage is limited for the HR grisms, observations in two different instrumental setups were often taken to cover the important spectral regions around  $H\beta$  and  $H\alpha$ .

Depending on the apparent angular sizes of the QSO host galaxies, we selected different magnifications of  $0''.33 \times 0''.33$  or  $0''.67 \times 0''.67$  per spaxel<sup>3</sup>. This yields a field-of-view (FoV) of  $13'' \times 13''$  or  $27'' \times 27''$  for the 1600 fibres arranged in a rectangular grid of  $40 \times 40$  spaxels. The total integration time per instrumental setup ranged between 900 s and 3150 s, split into at least 3 exposures. A dithering scheme allowed the rejection of dead fibres during data combination. The median seeing of all observations was  $1''.3$  and the median airmass was 1.2. Details on the individual observations are given in Table 2.

Unfortunately, a few QSOs were not properly centred in the VIMOS FoV because of the blind acquisition procedure, which affected observations in the high magnification mode ( $0''.33$  spaxels) more severely. Thus, HE 1201–2408 and HE 1434–1600 are only partially covered with our targeted VIMOS FoV and HE 1335–0847 is not covered at all with the HR orange grism setup. Observation of HE 1020–1022 suffered from poor photometric conditions resulting in an exceptionally bad spectrophotometry. The spectra of the HR orange and HR red observations do not match in the overlapping wavelength range, neither in slope nor in absolute calibration, so that we rejected this object from any detailed analysis in this paper.

## 2.3 Data reduction

We used a completely self-made reduction pipeline for the complex VIMOS data reduction, which is based on the reduction pipeline written in Python for the data of the Calar Alto Legacy Integral-field Area (CALIFA) survey (Sánchez et al. 2012a; Husemann et al. 2013a). The CALIFA pipeline can almost directly be applied to the VIMOS data with just a few dedicated modifications, because the CALIFA survey also uses a fibre-fed IFU similar to VIMOS. A key feature of the pipeline is the use of pixel tables and only applies resampling steps for the wavelength calibration and spatial resampling of the final cubes. The pipeline performs all basic reduction steps: Bias subtraction, automatic fibre identification with rejection of bad fibres, cosmic ray detection/rejection with PyCosmic (Husemann et al. 2012), straylight subtraction, fibre tracing, flexure correction, spectral extraction, wavelength calibration, fibre

flat-fielding and flux calibration. We provide a description of the different reduction steps below, including our special treatment for the VIMOS instrument and how the final data cubes are created from multiple exposures.

A master bias frame was created for each of the four independent spectrograph CCDs as the median of 5 bias frames regularly taken each day. These master bias frames were subsequently subtracted from all raw images. Automatic fibre identification often fails for VIMOS. We take the known low transmission (bad) fibres and the flexure offsets into account when automatically cross-matching the fibre peak positions with a VIMOS fibre position template. The fibre peaks were then traced along the dispersion axis. This process was robust except for the HR blue observations where the tracing was lost for a few fibres at the blue end ( $\lambda < 4300$ ) caused by their low transmission. We ignored that effect because that spectral region is unimportant for our scientific analysis.

Strong flexure is an important effect that varies with the position of the telescope. Thus, the traces of fibres in the continuum lamp exposure do not necessarily match with that of the science frames taken at slightly different telescope positions. To estimate the relative offsets between the traces in the science frames and the continuum exposure, we measured the fibre positions directly in the science frame by co-adding the light of 200 pixels along the dispersion direction at 5–6 locations distributed along the dispersion axis. Afterwards we extrapolated the measured offsets on to the entire dispersion axis using a Legendre polynomial of 2nd order. We find flexure offsets up to  $\pm 2.5$  pixels in cross-dispersion for the observations from 2004 and only  $\pm 0.5$  pixels for the observations from 2009 following an upgrade of the instrument. Flexure offsets are also expected to occur in the dispersion direction. We estimated those flexure offset from the difference between the measured and expected wavelength of prominent night sky emission lines. The offsets were then extrapolated to the entire wavelength range with a Legendre polynomial of 2nd order. However, only one sky line in the HR blue setup is bright enough to estimate the flexure offsets, so that we applied a 0th-order correction in that case. In addition, we correct the wavelength calibration for the heliocentric velocity shift of the target at the time of observation.

Each spectrograph of VIMOS covers 400 fibres densely projected on to each CCD so that cross-talk between fibres is an issue. We use an optimal extraction algorithm (Horne 1986) assuming a Gaussian profile in cross-dispersion for each fibre with fixed position and FWHM individually. The FWHM fibre profiles were determined independently for blocks of 20 fibres simultaneously at every 50th pixel in dispersion direction which is extrapolated along the dispersion axis with a lower order polynomial. Bad CCD pixels and cosmic ray hits are masked during the extraction process. The value of the extracted spectrum is flagged as bad, if the brightest 3 pixels of a fibre at a certain spectral pixel are bad. The error of each spectrum is computed with the optimal extraction algorithm based on the Poisson and read-out noise of each CCD pixel. At the end of the spectra extraction process, we store the data as a row-stacked spectra (RSS) file containing the spectra, wavelength, error and bad pixel masked as different extensions.

Afterwards, we adaptively smoothed the spectra to a common spectral resolution of  $3\text{Å}$  (FWHM) that were estimated from the FWHM of the lines in the arc lamp frame. This is important for modelling the continuum over the entire wavelength range and interpreting line width properly. All spectra are resampled to a common wavelength solution for each instrumental setup. We chose the sampling points for the different setups such that they are consistent in their overlapping wavelength range to allow a simple combi-

<sup>3</sup> spectral pixel, a single spatial resolution element containing a spectrum along the entire wavelength range



**Table 2.** VIMOS observational log.

Object	Date	Grating	Sampling	$t_{\text{total}}^a$	$n_{\text{exp}}^b$	Airmass	Seeing <sup>c</sup>	Resolution <sup>d</sup>	Remarks <sup>e</sup>
HE 0952–1552	2003–12–21	HR Orange	0''67	2700	6	1.1	1''0/1''5	2.0/3.0 kpc	
HE 1019–1414	2009–05–18	HR Blue	0''67	2000	4	1.0	0''9/1''5	1.2/2.1 kpc	
	2009–05–18	HR Orange	0''67	3000	4	1.1	1''1/1''6	1.5/2.2 kpc	
HE 1020–1022	2009–05–19	HR Orange	0''33	2000	4	1.1	0''9/1''4	2.9/4.5 kpc	(i)
	2009–05–13	HR Red	0''33	3000	4	1.2	1''2/1''6	3.8/5.0 kpc	(i)
HE 1029–1401	2003–12–17	HR Blue	0''67	900	3	1.1	1''0/1''5	1.6/2.4 kpc	
	2003–12–23	HR Orange	0''67	2700	6	1.2	0''9/1''5	1.4/2.4 kpc	
HE 1043–1346 <sup>†</sup>	2003–12–22	HR Orange	0''67	2700	6	1.2	1''2/1''6	1.6/2.1 kpc	
	2009–05–19	HR Blue	0''67	2000	4	1.2	1''1/1''6	1.4/2.1 kpc	
HE 1110–1910	2003–12–20	HR Orange	0''67	2700	6	1.1	1''0/1''5	2.0/3.0 kpc	
HE 1201–2408	2009–04–15	HR Orange	0''33	1500	2	1.1	...	...	(ii)
	2009–04–15	HR Red	0''33	1000	2	1.0	...	...	(ii)
HE 1228–1637	2003–12–30	HR Orange	0''67	3150	7	1.2–1.6	1''0/1''6	1.9/3.0 kpc	
HE 1237–2252	2003–12–31	HR Orange	0''67	2700	6	1.6–2.3	1''3/1''8	2.3/2.9 kpc	
HE 1239–2426	2003–12–28	HR Blue	0''67	900	3	1.5	1''3/1''6	1.9/2.4 kpc	
	2003–12–31	HR Orange	0''67	2700	6	1.2–1.5	1''2/1''4	2.8/2.1 kpc	
HE 1254–0934	2004–01–01	HR Orange	0''67	2700	6	1.4–1.8	1''2/1''5	2.7/3.6 kpc	
	2009–04–18	HR Red	0''67	2000	4	1.2	1''2/1''8	2.7/4.3 kpc	
HE 1300–1325	2009–04–22	HR Blue	0''67	2000	4	1.2–1.5	1''2/1''9	1.1/1.7 kpc	
	2009–04–25	HR Orange	0''67	3000	4	1.2	0''9/1''7	0.8/1.5 kpc	
HE 1310–1051	2009–04–22	HR Blue	0''67	2000	4	1.2	1''3/1''8	0.9/1.3 kpc	
	2009–04–25	HR Orange	0''67	3000	4	1.3–1.5	0''9/1''4	0.6/1.0 kpc	
HE 1315–1028	2004–01–17	HR Orange	0''67	3000	4	1.3–1.7	1''3/1''8	2.3/3.2 kpc	
HE 1335–0847	2009–04–24	HR Blue	0''33	2000	4	1.3–1.6	0''8/1''6	1.2/2.4 kpc	
HE 1338–1423	2009–04–27	HR Blue	0''67	2000	4	1.1	1''1/1''7	0.9/1.4 kpc	
	2009–04–27	HR Orange	0''67	3000	4	1.2–1.5	1''1/1''7	0.9/1.4 kpc	
HE 1405–1545	2004–01–22	HR Orange	0''67	2700	6	1.2–1.5	2''2/2''6	7.0/8.3 kpc	
	2004–01–27	HR Red	0''67	900	3	1.2	1''2/1''6	3.8/5.1 kpc	
HE 1416–1256	2009–04–18	HR Orange	0''33	3000	4	1.1	0''9/1''4	2.1/3.2 kpc	
HE 1434–1600	2009–04–17	HR Orange	0''33	1500	2	1.2–1.5	...	...	(ii)
	2009–04–18	HR Orange	0''33	1000	2	1.2	...	...	(ii)

<sup>a</sup>Total integration time of all exposures in seconds. <sup>b</sup>Number of exposures taken for a given object and instrumental setup.

<sup>c</sup>Estimated seeing of the combined cubes for the minor and major axis of the asymmetric VIMOS point spread function at the wavelength of the broad Balmer lines. <sup>d</sup>Physical spatial resolution at the redshift of the object according to the seeing.

<sup>e</sup>Objects marked with (i) are rejected from the analysis because of exceptionally bad spectrophotometry as explained in the text. Objects marked with (ii) were positioned at the edge of the VIMOS FoV so that an absolute photometric calibration could not be performed. <sup>†</sup>The HR Blue observation of HE 1043–1346 suffers from a bad spectrograph focus in the quadrant covering the QSO.

nation. Fibre-flats were created from the corresponding continuum lamp exposures for each object to correct differences in the fibre-to-fibre transmission. We find residual fibre-to-fibre variations of  $\pm 5$  per cent across the field as measured by the flux of the [OI]  $\lambda 5577$  night-sky line in blank sky fields. We note that those variations are significantly smaller than reported for other VIMOS IFU observations, e. g. up to  $\pm 30$  per cent (Arribas et al. 2008), which is most likely related to the fact that other VIMOS pipelines do not properly take into account the significant cross-talk.

Flux-calibration was performed based on spectroscopic standard star observations that were processed along the same steps outlined above. We computed a master sensitivity function for a given instrumental setup by averaging the sensitivity curves of all available standard star observations close to our science targets. The master sensitivity function was then used to perform a relative flux calibration of the science data.

We subsequently applied the following post-processing to create science ready datacubes. A mean sky spectrum was extracted from four spatial regions at the edges of the VIMOS FoV that were free from host galaxy emission, and they were subtracted them from all the spectra in each of the four quadrants separately to re-

move the background signal. We traced the positional change of the bright point-like QSO as a function of wavelength caused by the atmospheric dispersion. The different dithered science exposures were then registered with respect to the QSO position at a given wavelength and combined in a single step with the drizzle algorithm (Fruchter & Hook 2002). During the combination of dithered exposures bad pixels and bad fibres are masked. Thereby, we limit the spatial resampling steps to one while correcting for atmospheric dispersion at the same time. This allows the propagate of errors with least correlated noise.

To establish an absolute flux calibration, we matched the synthetic *V*-band photometry of the VIMOS data with the *V*-band photometry of the ground-based images taken from Jahnke, Kuhlbrodt & Wisotzki (2004). The spectra were also corrected for Galactic extinction assuming the attenuation law of Cardelli, Clayton & Mathis (1989) together with the corresponding *V* band extinction ( $A_V$ ) along the line-of-sight for each object measured by Schlegel, Finkbeiner & Davis (1998). Finally, we removed the telluric absorption bands with a normalized absorption template generated from the standard star observations.

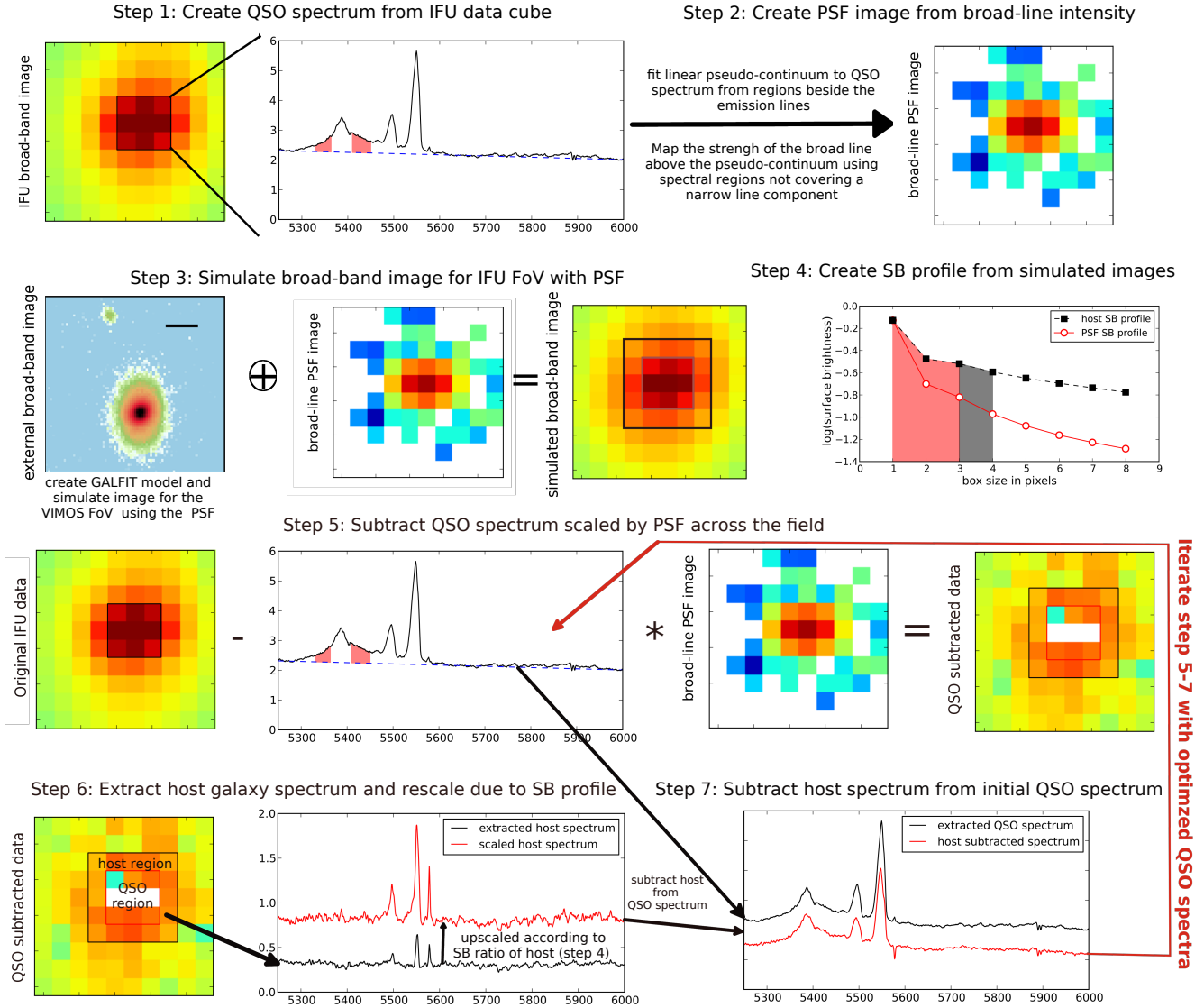


**Figure 1.** Sketch to illustrate the various steps of the iterative algorithm to deblend the QSO from the host galaxy emission with QDEBLEND<sup>3D</sup>.

### 3 SPECTRAL QSO-HOST DEBLENDING IN 3D

#### 3.1 Applying QDEBLEND<sup>3D</sup> to VIMOS data

Studying the properties of QSO host galaxies, and type 1 AGN hosts in general, requires a robust deblending of the AGN and host galaxy light. In the case of 3D spectroscopy, this deblending needs to be done in the spatial *and* spectral dimensions, for which a dedicated algorithm is needed. We presented a dedicated software tool QDEBLEND<sup>3D</sup> for this task<sup>4</sup> in Husemann et al. (2013b), which is an improved version of the iterative algorithm initially presented by Christensen et al. (2006) to detect extended Ly $\alpha$  emission in IFU data of high-redshift QSOs. The basic concept of QDEBLEND<sup>3D</sup> is that the spectrum in each spaxel is a superposition of the host galaxy spectrum at this position and of the AGN spectrum modulated in absolute flux according to the point-spread function (PSF) of the observation. Although current integral field spectrographs

usually do not capture stars simultaneously with the target, given their small FoV, type 1 AGN offer the opportunity to self-calibrate a PSF based on their broad emission lines (Jahnke et al. 2004b). More details about QDEBLEND<sup>3D</sup> and its algorithm can be found in Husemann et al. (2013b) or in the user manual of QDEBLEND<sup>3D</sup>. Here, we briefly outline the process and show a sketch of the different steps in Fig. 1 to illustrate the iterative algorithm of QDEBLEND<sup>3D</sup> applied to our QSO observations.

In the first iteration, a high S/N co-added QSO spectrum is extracted from a  $3 \times 3$  spaxels region centred on the brightest QSO spaxels (step 1). The broad emission-line originate from the QSO broad-line regions on scales of a few pc or less and will appear as a point source in our observations. We measure the relative brightness of the broad-line wings against the local pseudo-continuum to reconstruct the PSF of the IFU observations (step 2). We simulate a broad-band image for the exact VIMOS FoV and PSF based on a host galaxy model obtained from a nucleus-to-host decomposition with GALFIT of an available broad-band image (step 3). Then we create a SB profile of the host galaxy (step 4) that we use later

<sup>4</sup> available for download at <http://sourceforge.net/projects/qdeblend/>

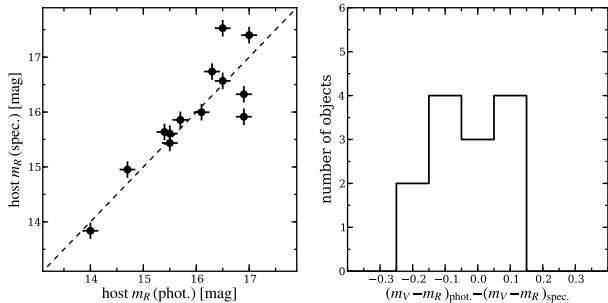


**Figure 2.** Photometric comparison of our host galaxy spectra with the archival broad-band photometry of Jahnke, Kuhlbrodt & Wisotzki (2004). *Upper panel:* Synthetic  $R$  band magnitudes of our deblended host galaxy spectra against the photometric ones.  $3\sigma$  error bars are shown as inferred from dedicated Monte Carlo simulation presented in the appendix. *Lower panel:* Histogram of the  $V - R$  colour difference between our spectroscopic and broad-band photometric data.

in the iterative process. A pure QSO datacube is constructed by scaling the high S/N QSO spectrum to match the flux in the broad-line wings in each spaxel. The QSO datacube is then subtracted from the original cube and is supposed to contain only host galaxy emission (step 5). However, the initially extracted QSO spectrum is inevitably contaminated by some host galaxy light. We iteratively remove that host galaxy contribution with QDEBLEND<sup>3D</sup>. In four subsequent iterations, we extract a host galaxy spectrum from a single spaxel wide annulus *around* the central QSO region ( $3 \times 3$  spaxels) from the QSO-subtracted datacube (step 6). Since the radial SB gradient of the PSF is much steeper than that of the host galaxy, the annulus is dominated by host galaxy light after the QSO subtraction. We rescale the host galaxy spectrum to match the expected host galaxy surface brightness *within* the QSO region as determined from the 2D SB profile (estimated in step 4) before we subtract it from the initial QSO spectrum to be used for the next iteration (step 7).

Although the FWHM of the PSF changes slowly with wavelength, we could only estimate a PSF at the observed wavelength of  $H\beta$  and  $H\alpha$ . We therefore split the datacubes when both lines were covered in a single observation. The separated datacubes were then individually processed and combined again at the end. The remaining PSF mismatch at wavelengths far away from the Balmer lines does affect the recovered slope in the stellar continuum for spaxels close to the QSO position. However, our attention is focused on the emission lines of the ionized gas within  $\sim 200\text{\AA}$  from the Balmer lines in this paper for which such a PSF mismatch is not significant.

### 3.2 Results and quality check

The decomposed spectra of all are shown in Fig. B1 in Appendix B to show the results of the spectral deblending process. Because of the limited sensitivity of our observations we recovered the stellar continuum emission of the host galaxy for all objects except HE 1201–1201, HE 335–0847, HE 1416–1256 and HE 1434–1600. For the majority of objects, however, we recovered various prominent stellar absorption lines in the continuum. No remaining residuals of the broad emission lines are seen in the host galaxy spectra as a clear signature for the reliable separation of host and QSO light using QDEBLEND<sup>3D</sup>.

To roughly test the quality of the host galaxy spectra, we compare the broad-band photometry with our spectroscopy data in

Fig. 2 for a consistency check. We find that the  $V$  and  $R$  broad-band magnitudes computed from our host galaxy spectra are in agreement with the photometric host magnitudes of the multi-colour images (Jahnke, Kuhlbrodt & Wisotzki 2004) within their  $3\sigma$  uncertainties. We determined the error from dedicated Monte Carlo simulations as described in the appendix A. Here, we assume that the errors are similar for both data sets since the uncertainties are dominated by the systematics of the QSO-host deblending process. Additional uncertainties from the complex VIMOS flat-fielding are not included in the simulation. We expect that this effect is small because we find very little systematic offsets.

Significant scatter in the absolute photometry occurs mainly for the faintest host galaxies with  $m_R \gtrsim 16.5$  where the S/N of the IFU becomes critical for the QSO-host deblending process, but it is still consistent within the errors. Considering the  $V - R$  colours, we find a very good agreement with respect to the multi-colour imaging data with a colour difference of typically  $\pm 0.1$  mag except two cases. This is a more quantitative indication that the shape of the underlying stellar continuum is not significantly contaminated by emission from the QSO nucleus.

### 3.3 Estimation of measurement and systematic uncertainties

The deblending process is not free from random and systematic uncertainties. Certain wavelength regions covering either the QSO broad emission lines or their adjacent continuum were *manually* selected such that no residual broad line was apparently visible in the host galaxy spectrum. Small changes in those selected wavelength regions may have a significant impact on the result. We incorporated this effect in the error analysis via a Monte-Carlo approach.

We generated 500 Monte-Carlo realizations for each observed datacube for which we changed the flux in each pixel within the error distribution as inferred from the variance cube. The deblending process was then applied to each realization exactly in the same way as the observed data, except that the boundaries of the manually selected wavelength regions were randomly varied within  $\pm 10$  assuming a flat distribution. An additional constraint was that the new wavelength regions have a width of at least  $2\text{\AA}$ , otherwise new boundaries were randomly chosen to match this criterion.

Total host and QSO spectra were extracted and stored from the 500 deblended realizations, which we used to estimate the measurement errors of the integrated spectra. The first 50 datacubes of each Monte Carlo run were fully stored for the error analysis of the *spatially resolved* QSO host properties.

Apart from the measurement errors, the QSO-host deblending process is also subject to systematic uncertainties. We perform extensive simulation to study the systematic effects of the process on the main quantities we obtain from our observation. We create realistic IFU data at the redshifts of our QSOs based on existing IFU data of very nearby galaxies from the CALIFA survey (Sánchez et al. 2012a). Details of the simulations and their results are presented in Appendix A.

## 4 EMISSION-LINE DIAGNOSTICS OF THE IONIZED GAS

### 4.1 Estimating the stellar continuum

Before analysing the emission lines of the ionized gas, the stellar continuum had to be subtracted because the Balmer emission lines can be heavily blended with the corresponding stellar absorption

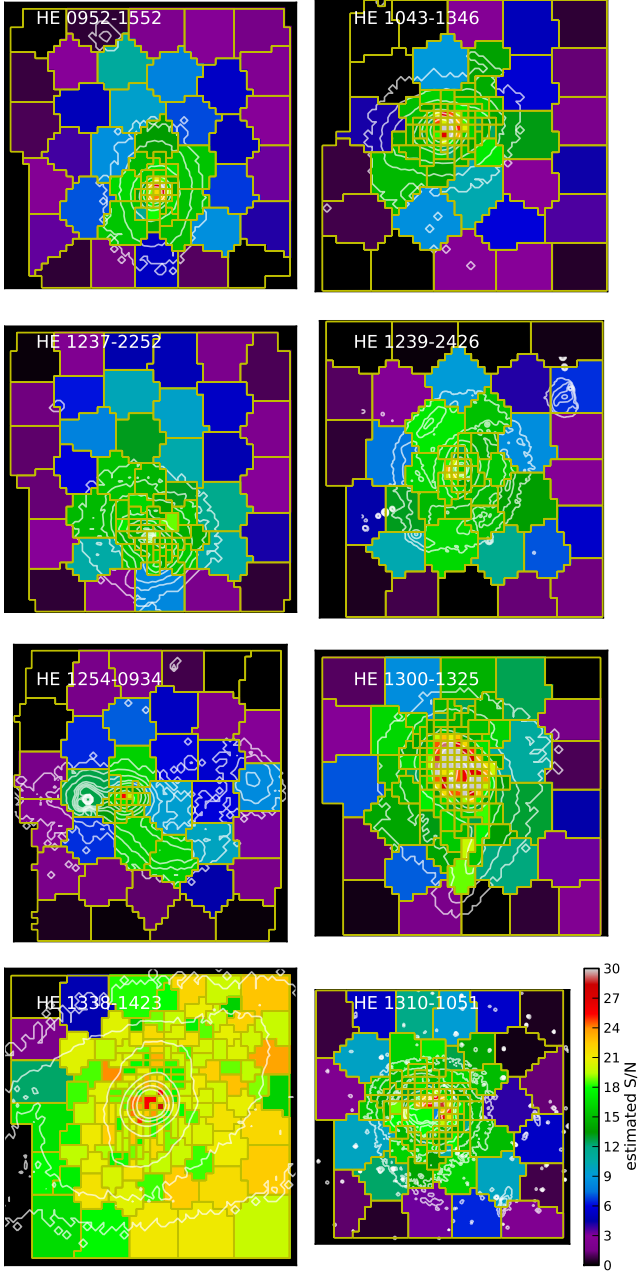


**Figure 3.** Results of the Voronoi binning for all host galaxies with sufficient extended continuum S/N. The colour maps represent the estimated S/N of the host spectrum after binning of spaxels. The broad-band surface brightness distribution of the host galaxies is indicated by white contours.

lines. One possibility to estimate an appropriate stellar continuum spectrum is to find the best linear combination of a set of stellar template spectra. We used the spectral synthesis code STARLIGHT (Cid Fernandes et al. 2005) for this purpose. STARLIGHT searches for the best linear combination of template spectra taking into account the effect of reddening ( $A_V$ ), smooths the templates to the optimal stellar velocity dispersion ( $\sigma_*$ ), and shifts them to the systematic velocity ( $v_*$ ) matching the observed spectrum ( $O_\lambda$ ) in terms of kinematics and overall shape. Comparing the model spec-

tra ( $M_\lambda$ ) with the observed spectrum ( $O_\lambda$ ), STARLIGHT searches for the minimum of

$$\chi^2 = \chi^2(\vec{a}, A_V, v_*, \sigma_*) = \sum_{\lambda} ((O_\lambda - M_\lambda) w_\lambda)^2 \quad (1)$$

The weights  $w_\lambda$  are the inverse errors of the observed spectrum. We specifically doubled the weights for the spectral regions around the G-band and MgI  $\lambda 5166$  absorption lines to improve the kinematic measurements and set the weights to zero for every spectral region containing prominent emission lines.

The high spectral resolution single stellar population (SSP) library generated by González Delgado et al. (2005) from a library of synthetic stellar spectra (Martins et al. 2005) served as our template spectra. We selected a set of 39 different SSPs with ages of 1, 3, 5, 10, 25, 40, 100, 300, 600, 900, 2000, 5000 and 10000 Myr and metallicities  $2Z_\odot$ ,  $1Z_\odot$ , and  $0.2Z_\odot$ . Additionally, we used a set of 15 stellar spectra ranging in spectral type from O to K from the Indo-U.S. library (Valdes et al. 2004) at a spectral resolution of  $\sim 1\text{\AA}$  to check the reliability of the results and to estimate systematic uncertainties related to the choice of the template library.

The spectrum of the best-fitting combination of SSP spectra for the integrated QSO host galaxy spectra is shown in the bottom panels of Fig. B1 in the Appendix. Although we performed an integration over the entire host galaxy, the continuum is mainly dominated by the bright central region of the galaxy. In most cases, we find a good match between the observed and modelled continuum in most cases, considering that the bright QSO emission had to be removed before.

For the present article, we solely focus on measuring emission line fluxes from the ionized gas for diagnostic purposes. Although this requires a good representation for the continuum spectra, an accurate determination of the stellar population parameters and star formation histories is not required. However, well known degeneracies of stellar populations parameters, like the age-metallicity degeneracy (Worthey 1994), reduce the ability to accurately recover the age of the stellar population (e.g. Cid Fernandes et al. 2004). We tested whether these degeneracies significantly affect the robustness of our emission line measurements by comparing the continuum subtracted  $H\beta$  fluxes of all our host spectra based on two synthetic stellar library spectra. We found that the scatter in the  $H\beta$  flux is only  $\simeq 0.05$  dex, so that our emission-line measurements are robust and independent of the chosen stellar library for our observations to first order.

The modelling of the stellar continuum could often be extended to a spatially resolved scheme for the bright disc-dominated QSO host galaxies in our sample. Because the S/N of the individual spaxels are in most cases below 10, we employed weighted Voronoi tessellations (Diehl & Statler 2006) to adaptively bin adjacent spaxels. This is a generalization of the Voronoi binning algorithm of Cappellari & Copin (2003), which has been widely used in the IFU community (e.g. Emsellem et al. 2004; Sarzi et al. 2006; McDermid et al. 2006; Gerssen et al. 2006; Dumas et al. 2007; Stoklasová et al. 2009; Cid Fernandes et al. 2013). We estimated a S/N map directly from the data by measuring the mean and standard deviation in the rest-frame spectral window of  $5500 < \lambda < 5700$ . This is a conservative S/N estimate due to the presence of some weak absorption lines in that wavelength range. We chose a target S/N of 20 per bin for the brightest galaxy HE1338–1423 and a target S/N of 15 for the rest of galaxies. We limited the maximum number of spaxels per bin to 50 for the weighted Voronoi algorithms. The resulting S/N maps after binning are shown in Fig. 3 for all galaxies with sufficiently extended continuum signal. When less than 5 bins had

**Table 3.** Stellar continuum subtraction schemes

Object	$\log L_{5100}^a$ [erg/s]	$\log L_{[\text{OIII}]}^b$ [erg/s]	$r_e^c$ [kpc]
HE 0952–1552	$43.98 \pm 0.09$	$41.88 \pm 0.10$	$3.4 \pm 0.1$
HE 1019–1414	$43.40 \pm 0.11$	$41.94 \pm 0.11$	$1.9 \pm 0.1$
HE 1029–1401	$44.94 \pm 0.09$	$42.39 \pm 0.11$	$4.5 \pm 0.1$
HE 1110–1910	$44.05 \pm 0.10$	$41.66 \pm 0.11$	$3.2 \pm 1.1$
HE 1228–1637	$44.08 \pm 0.10$	$41.67 \pm 0.14$	$<1.8$
HE 1237–2252	$43.44 \pm 0.11$	$41.22 \pm 0.13$	$2.4 \pm 0.3$
HE 1239–2426	$43.81 \pm 0.10$	$41.20 \pm 0.11$	$1.9 \pm 0.1$
HE 1254–0934	$44.68 \pm 0.11$	$42.53 \pm 0.12$	$3.8 \pm 0.1$
HE 1300–1325	$43.46 \pm 0.09$	$41.23 \pm 0.09$	$<1.4$
HE 1310–1051	$43.55 \pm 0.10$	$41.66 \pm 0.14$	$<1.9$
HE 1338–1423	$43.73 \pm 0.10$	$42.00 \pm 0.13$	$2.0 \pm 0.0$
HE 1405–1545	$44.22 \pm 0.11$	$42.03 \pm 0.12$	$4.6 \pm 0.1$
HE 1416–1256	$44.13 \pm 0.12$	$42.85 \pm 0.11$	$5.6 \pm 0.5$

<sup>a</sup>QSO continuum luminosity at 5100 after removing the contribution from the host galaxy. <sup>b</sup>Integrated [OIII] luminosity from the unresolved QSO and extended ENLR. <sup>c</sup>[OIII] luminosity-weighted effective ENLR radius excluding the HII-like regions. Upper limits are derived for those objects which do not show an ENLR and represent the shortest distance to an HII-like region.

a S/N in the continuum greater than 15, we decided to use only the model of the integrated spectrum as a global continuum template spectrum for all spaxels. For a few objects, mainly those observed with  $0''.33$  spatial resolution, no significant stellar continuum light could be recovered for subtraction. Table 3 indicates which of those three schemes were applied to a specific object.

After binning, we modelled the co-added stellar continuum of each bin with STARLIGHT again as described above for the integrated spectra. Because the seeing often changed between observations of different instrumental setups, the absolute continuum flux level for small bins (e.g. a single spaxel) may not necessarily be the same for the consecutive spectra. We therefore normalized the spectra of the two instrumental setups to match in the overlapping spectral region before combination.

Pure emission-line datacubes were subsequently created by subtracting the best-fitting continuum model, either spatially resolved or based on the model of the integrated spectrum. The corresponding continuum model was scaled in absolute flux before subtraction to match that of each individual spaxel. We repeated the process for our 50 Monte Carlo realizations, previously constructed during the QSO-host deblending process, to generate 50 pure emission-line datacubes that we used to estimate the systematic uncertainties of the continuum subtraction on the emission line measurements.

## 4.2 Narrow-band images

After removing the QSO emission and the underlying stellar continuum, we extracted  $20\text{\AA}$  wide narrow-band images (Fig. 4, left panel) from the datacubes centred on the strongest emission lines, H $\alpha$  (or H $\beta$  in the case of HE 1335–0847) and [OIII]  $\lambda 5007$  (hereafter [OIII]), to characterize the spatial distribution of the ionized gas. These images reveal the presence of extended ionized gas in almost all QSO host galaxies.

In comparison with the broad-band continuum images, particularly the high-resolution *HST* images, we find that the H $\alpha$  emission in most cases tracks very nicely the substructures in the

morphology of the host galaxies. For example, the high surface brightness knots in the *HST* ACS F606W broad-band images of HE 1043–1346 and HE 1239–2426 seen along the spiral arm and close to the nucleus coincide with the observed pattern of strong H $\alpha$  emission. The H $\alpha$  image of HE 1338–1423 shows strong residuals close to the nucleus. The QSO-host deblending is particularly difficult for the HR orange observation of this object. The broad H $\alpha$  emission line of the QSO is rather narrow ( $\sim 1600 \text{ km s}^{-1}$  FWHM) and the extended [NII]  $\lambda\lambda 6548, 6583$  and H $\alpha$  emission lines are bright so that it was impossible to define broad line spectral windows that are not contaminated by extended emission across the entire field.

The distribution in the ionized gas traced by the H $\alpha$  and [OIII] lines is often consistent with each other, suggesting that a common ionization mechanism dominates throughout a galaxy. In a few galaxies, the [OIII] emission is rather weak or even undetected compared to H $\alpha$  (e.g. HE 1239–2426) which is typical for high metallicity HII-like regions. HE 0952–1552 and HE 1254–0934, on the other hand, display quite different light distributions in H $\alpha$  and [OIII] which presumably point to significant changes in the properties of the ISM across these galaxies.

## 4.3 Emission-line fluxes of specific regions

To investigate the physical conditions of the ISM in more detail, the fluxes of weaker emission lines, such as H $\beta$ , [NII]  $\lambda\lambda 6548, 6583$  and [SII]  $\lambda\lambda 6716, 6731$ , need to be accurately measured. Those lines are often too weak to be detected in individual spaxels, which requires a spatial binning of specific regions to increase the S/N. We manually defined several apertures (marked as black regions in Fig. 4), covering a physically connected region as judged from the H $\alpha$  or [OIII] light distribution.

We then modelled the emission-lines in the co-added spectrum of each aperture with simple Gaussians. Line ratios of the [OIII]  $\lambda\lambda 4960, 5007$  and [NII]  $\lambda\lambda 6548, 6583$  doublets were fixed to their theoretical values. All emission lines, H $\beta$ , [OIII]  $\lambda\lambda 4960, 5007$ , H $\alpha$ , [NII]  $\lambda\lambda 6548, 6583$  and [SII]  $\lambda\lambda 6716, 6731$  were modelled simultaneously, and their line dispersions and redshifts were coupled to common values. This approach strongly reduced the number of free parameters and increased the robustness of the best-fitting model. We used a downhill simplex algorithm to find the best-fitting parameters at the minimal  $\chi^2$ .

With a spectral resolution of  $\lambda/\Delta\lambda \sim 2500$ , corresponding to  $\sim 100 \text{ km s}^{-1}$  FWHM, we were able to resolve emission line systems with different kinematic components. This is important to disentangle the emission of companion galaxies along the same line-of-sight as the host galaxy, or for separating potential outflowing/inflowing gas associated with mergers, star formation, or AGN activity. We show in Fig. 5 two examples of the spectral emission line modelling that required two different emission line systems.

We derive the emission line errors on all parameter by analysing the 50 Monte-Carlo realizations of the datacubes and taking the standard deviation from the results. In this way we included the uncertainties of the QSO-host deblending and of the continuum subtraction into the error budget of the emission line measurements. We inferred  $3\sigma$  upper limits for undetected H $\beta$ , [OIII] or [NII] lines based on the noise from the adjacent continuum and the line width constrained by the detected lines.

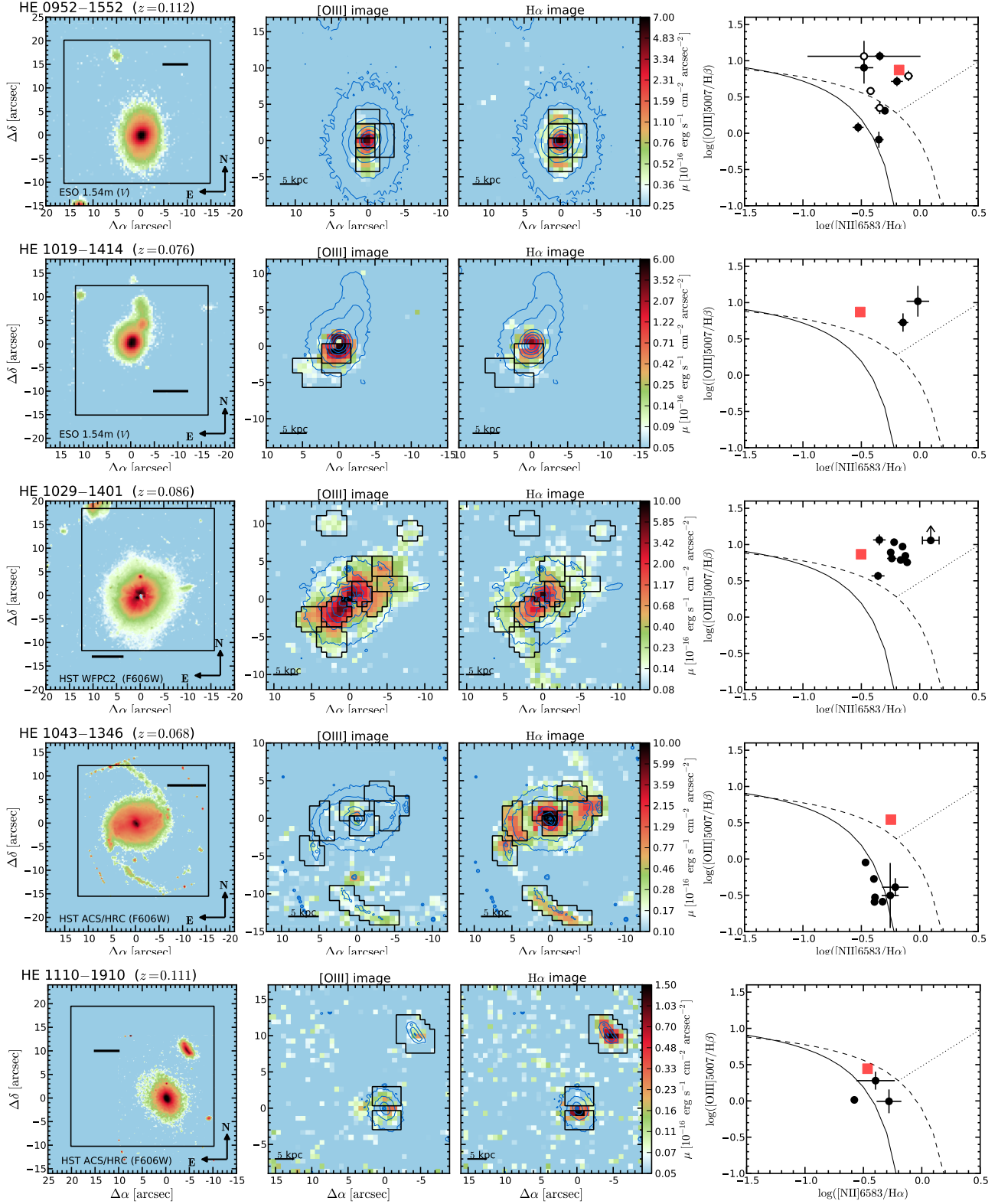


**Figure 4.** Sample overview of the emission-line characteristics after QSO subtraction. *Left panel:* QSO subtracted broad-band images of the host galaxies with the VIMOS FoV indicated by the rectangle. The black scale bar corresponds to 10 kpc at the redshift of the QSO. *Mid panel:* QSO and continuum subtracted [OIII] and H $\alpha$  narrow-band images in a logarithmic scaling. Apertures of specific regions are indicated by the black border lines and labelled alphabetically. Contours of the broad-band continuum surface brightness are over-plotted in blue to aid direct comparison. *Right panel:* Standard BPT diagram for the individual regions indicated on the broad-band images. A second kinematic system of emission-lines in those regions are indicated by open symbols if present. The red squared symbol corresponds to the line ratios of the narrow lines above the broad lines in the QSO spectrum as extracted from the brightest spaxel at the QSO position. The solid line is the demarcation curve for star-forming galaxies of Kauffmann et al. (2003), the dashed line is the theoretical maximum starburst line of Kewley et al. (2001) and the dotted line represents the boundary between Seyfert and LINER-like emission proposed by Cid Fernandes et al. (2010).



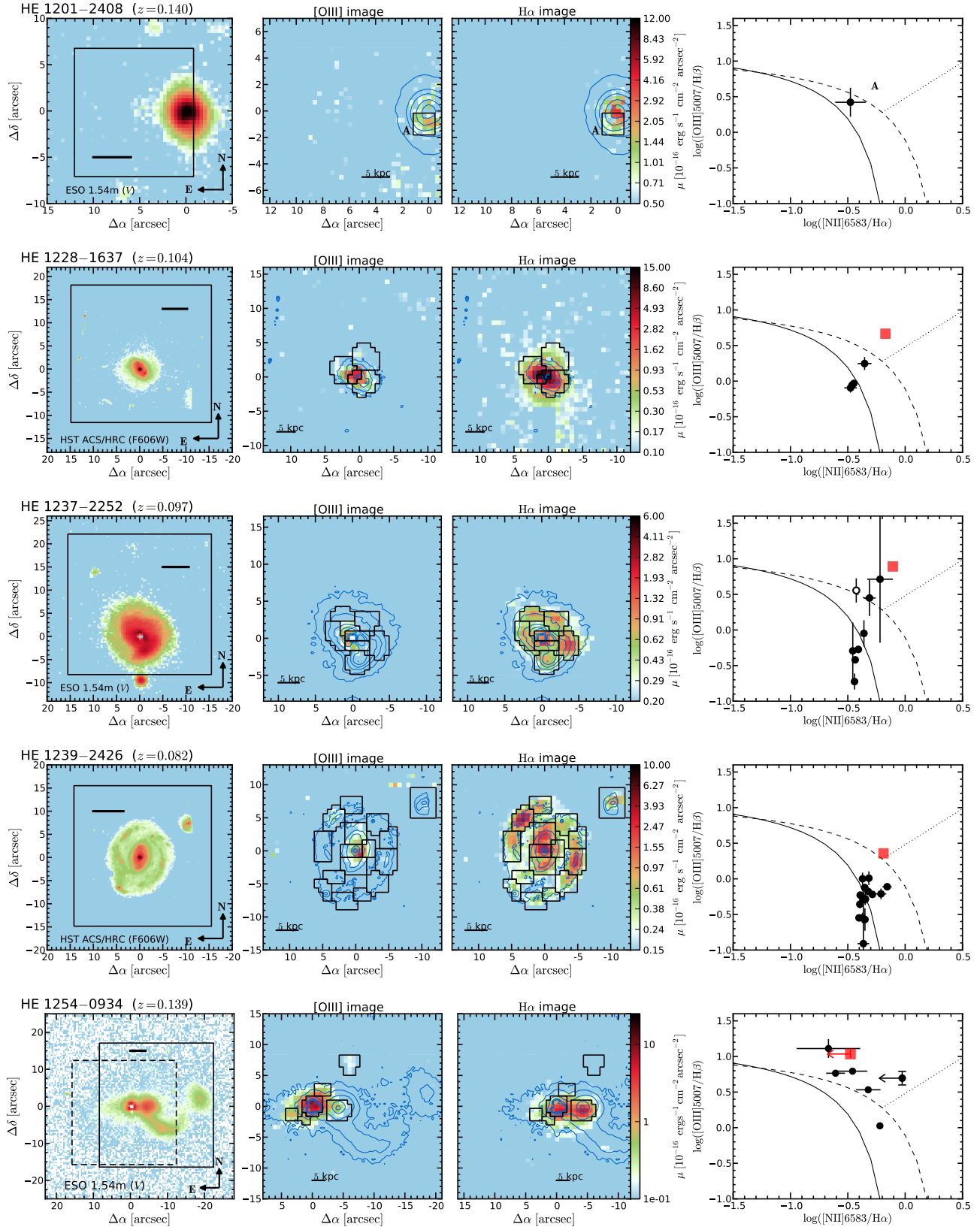


**Figure 4 – continued** The line ratios of the narrow lines in the QSO spectrum of HE 1201–2408 could not be robustly measured because the narrow [NII] lines could not be resolved above the broad H $\alpha$  line. The HR orange (solid line) and the HR red (dashed line) observations of HE 1254–0934 have slightly different FoVs with a substantial overlap.

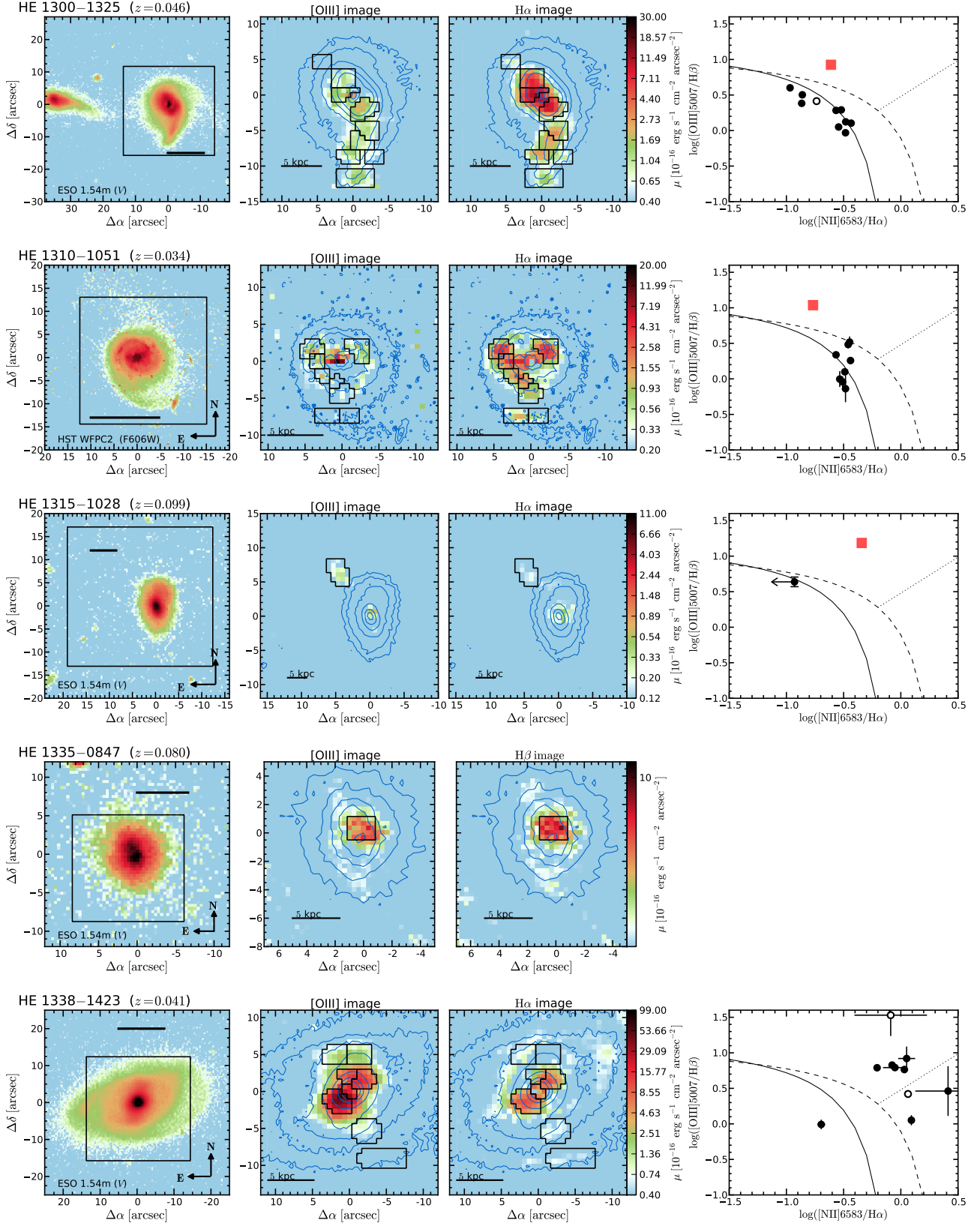


**Figure 4** – *continued* The line ratios of the narrow lines in the QSO spectrum of HE 1338–1423 could not be robustly measured because the narrow Balmer lines could not be well resolved above the broad Balmer lines in this case.



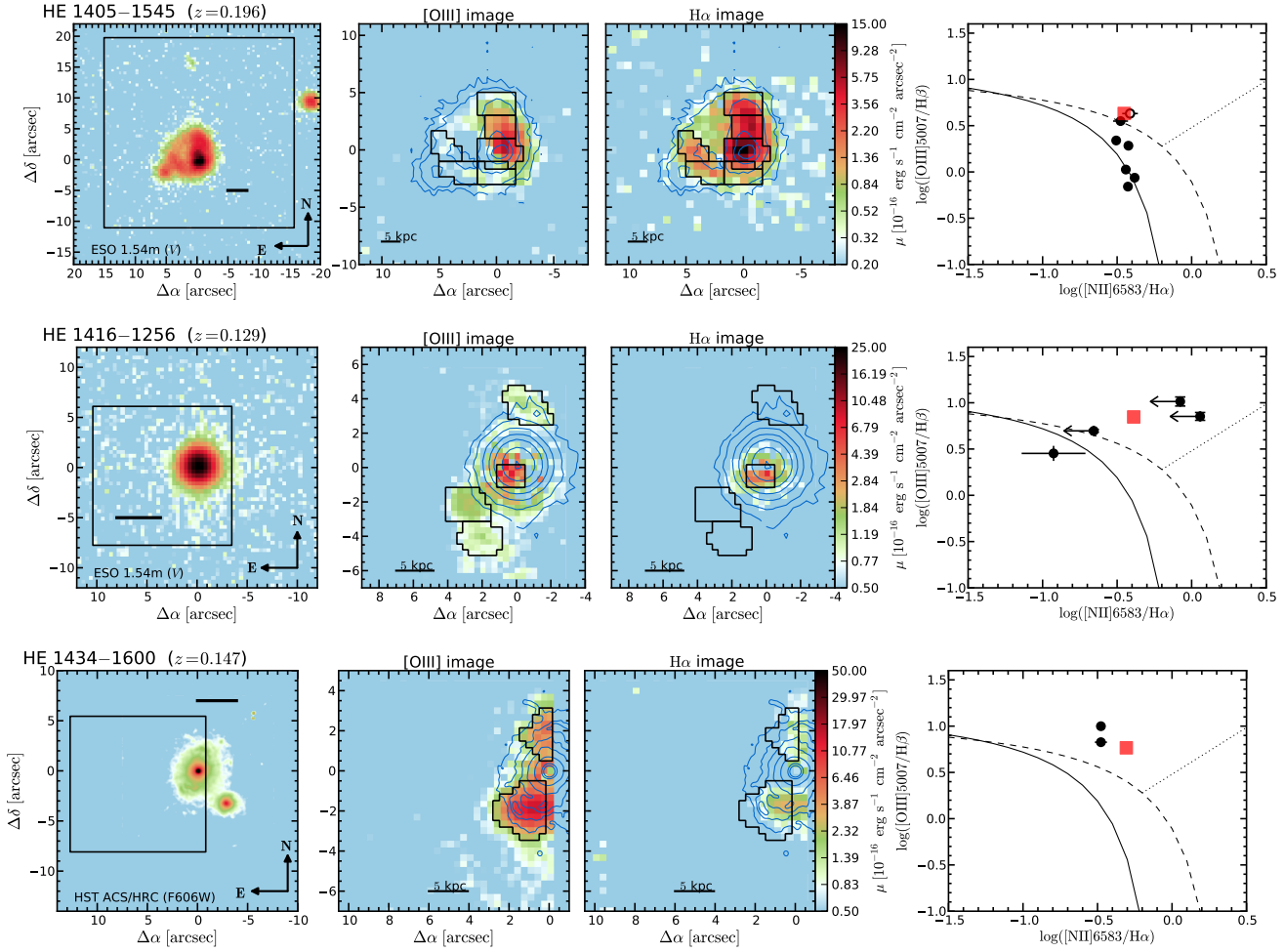


Figure 4 – continued

#### 4.4 Distinguishing HII-like and AGN ionization regions

Emission-line diagnostic diagrams have been used to constrain the dominant ionizing source of the ISM in galaxies. The most frequently used one is the  $[\text{OIII}]\lambda 5007/\text{H}\beta$  vs.  $[\text{NII}]\lambda 6582/\text{H}\alpha$  diagram, often referred to as the BPT diagram (Baldwin, Phillips & Terlevich 1981). It involves only emission-line ratios of the brightest lines in the rest-frame optical that are least sensitive to reddening. Several demarcation lines were proposed for the BPT diagram to discriminate between different underlying ionization mechanisms.

Kewley et al. (2001) derived a boundary for the BPT up to which it could theoretically be produced by a massive starburst. An empirical boundary for star-forming galaxies was drawn by Kauffmann et al. (2003) to include galaxies of the apparent star-forming branch in the SDSS data. These two demarcation curves have often been invoked to discriminate between star-forming or HII-like regions, gas predominantly ionized by an AGN, and an intermediate region where both processes may significantly contribute to the ionization. However, those demarcation curves cannot be hard boundaries and there would be a homogeneous sequence crossing those boundaries due to different levels of mixing. This implies that line ratios in the intermediate region could be well produced entirely by a starburst, and line ratios in the AGN branch might still be substantially contaminated by star-forming regions as discussed

by Cid Fernandes et al. (2010). Furthermore, shocks generated by jet-cloud interactions and their precursors can be another source of ionization in AGN host galaxies (e.g. Morganti et al. 1997; Clark et al. 1998; Villar-Martín et al. 1999; Moy & Rocca-Volmerange 2002; Rosario et al. 2010) for which the BPT line ratios significantly overlap with the other ionization mechanisms.

We present the BPT diagrams for emission-line regions across the host galaxy after the QSO-host deblending in Fig. 4 (right panels) of all the objects in our sample. The HR orange observation, covering the  $\text{H}\alpha$  and  $[\text{NII}]$  lines, is missing for HE 1335–0847, so that we could not construct a BPT diagram for this object. Nevertheless, we obtain a low  $[\text{OIII}]/\text{H}\beta$  line ratio of 0.3 for its prominent emission-line region which is consistent with an HII-like region. In the case of HE 1315–1028 and HE 1416–1256, the  $[\text{NII}]$  lines are undetected and we can provide only upper limits for the  $[\text{NII}]/\text{H}\alpha$  line ratio. In addition, we show the measured line ratios of the narrow lines above the broad lines in the QSO spectrum extracted from the brightest spaxel at the QSO position in Fig. 4 (right panels) as red squared symbols.

The BPT diagrams reveal that the ionization state of the ISM is diverse and sometimes changes even across the host galaxy. In the following we consider BPT line ratios below or close to Kauffmann et al. (2003) line to be dominated by HII-like regions indicative of ongoing star formation, and line ratios above the Kewley et al.

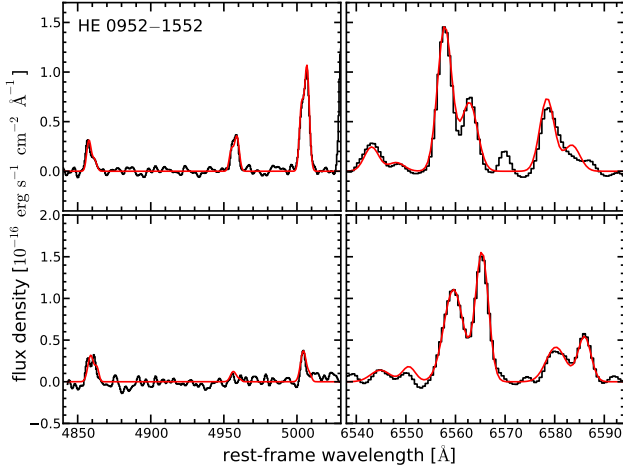


**Figure 5.** Examples of spectra requiring two kinematically distinct emission-line systems. A spectrum of HE 0952–1552 (region F) is presented in the top panels and a spectrum of HE 1237–2252 (region C) in the bottom panels. The red line represents the best-fitting model consisting of Gaussians for the various emission lines that are kinematically coupled to represent two independent emission line systems.

(2001) to be dominated by ionization through AGN photoionization or AGN driven shocks.

The narrow emission-line ratios in the QSO spectrum close to the nucleus are always in the region of AGN photoionization as expected also from other samples of luminous nearby AGN (e.g. Winter et al. 2010). How far AGN photoionization is dominating the gas ionization inside the host galaxy depends primarily on the AGN luminosity (e.g. Bennert et al. 2002) and other ionization mechanisms such as star formation will take over at some point. Despite the obvious radial dependence on the mixing between star formation and AGN photoionization in the emission lines, there is also a connection with the spectral properties of the QSO independent of luminosity (Husemann et al. 2008). QSOs with strong  $\text{FeII}$  emission and broad lines with  $\text{FWHM} < 4000 \text{ km s}^{-1}$  seem to be deficit of extended AGN photoionization for still unknown reasons, which complicates the simple picture.

On kpc scales across the host galaxies, we identified clear evidence for ongoing star formation in 10 out of 18 host galaxies, showing HII-like emission. In combination with the morphological classification, these numbers split up into 4/8 (50 per cent) for bulge-dominated QSO hosts, 5/8 (62.5 per cent) for disc-dominated QSO hosts and 1/2 (50 per cent) for major-merger systems. If we assume that the emission-line ratios in the intermediate region of the BPT have indeed contributions by HII-like regions, the number of QSO hosts with evidence for current star formation increase by 3 objects including the second major-merger system. On the other hand, we find evidence for AGN photoionization on kpc scales also in 10 out of the 18 cases, which occurs in at least 3 QSO hosts together with ongoing star formation at different locations.

The fact that we find only very few regions with intermediate line ratios suggests that the spatial resolution helps to reduce mixing effects compared to single fibre spectroscopy, so that regions of a given ionization mechanism are spatially separated. Also, LINER-like emission (Heckman 1980) for which the dominant ionization mechanism is strongly debated does not play a role for our study as all regions but one are above the corresponding demarcation line presented by Cid Fernandes et al. (2010).

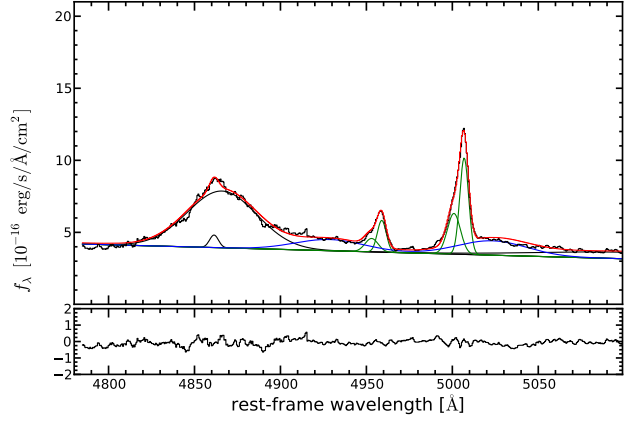


**Figure 6.** Multi-component fit to the QSO spectrum of HE 1043–1346 in the  $\text{H}\beta$ -[OIII] spectral region. The best-fitting model is indicated by the red solid line and the individual Gaussian components are plotted above the local linear continuum with the following colour coding: black –  $\text{H}\beta$  line, green – [OIII] doublet lines, blue –  $\text{FeII}$  doublet lines. The residuals of the model are shown in the lower panel with a refined scaling.

#### 4.5 Extended narrow-line region sizes and QSO luminosities

The [OIII] line is the brightest optical narrow emission line in case of AGN photoionization and can extend up to several kpc from the AGN, the so-called extended narrow-line region (ENLR, Unger et al. 1987). We constructed [OIII] narrow-band images from the QSO-subtracted IFU datacubes to measure the characteristic sizes of their ENLRs. Here, we estimated the sizes in the same manner as in our previous study on the ENLR around luminous low-redshift QSOs (Husemann et al. 2013b). All pixels below the  $3\sigma$  background noise level of the narrow-band image were masked out as well as all previously confirmed HII-like regions, but no region with intermediate line ratios. We then measured the effective ENLR radius ( $r_e$ ) as the luminosity-weighted radius of all unmasked pixels. Here, we do not use the maximum ENLR size, because it would be more likely affected by the low surface brightness features that are very sensitive to the depth and seeing of the observations.

In several cases, the extended emission lines are solely dominated by HII-like emission even close to the QSO at our spatial resolution. We provide upper limits on the ENLR size in these cases based on the smallest distance to a detected HII-like region. The objects HE 1201–2409 and HE 1315–1028 were excluded from this analysis because the ionization source of the ISM could not be unambiguously constrained. The ENLR of HE 1434–1600 is only partially covered by our observations and a robust size could also not be estimated.

The debleded datacubes also provide high S/N spectra of the QSOs that are uncontaminated from host galaxy emission. For the purpose of this paper, we only inferred the QSO continuum luminosity at  $5100\text{\AA}$  ( $L_{5100}$ ) and the [OIII] line luminosity ( $L_{[\text{OIII}]}$ ) from the spectra. We modelled the spectral region around the broad  $\text{H}\beta$  line with a set of Gaussians for the narrow and broad emission lines plus an underlying local continuum as described in Husemann et al. (2013b). Two Gaussians were usually required to account for the asymmetry of the [OIII] line profile. An example of the QSO spectral modelling is shown in Fig. 6 for illustration. The measured QSO continuum luminosities, integrated [OIII] luminosities of the QSO and ENLR are reported in Table 4 together with the effective ENLR sizes.

**Table 4.** QSO and ENLR properties

Object	$\log L_{5100}^a$ [erg/s]	$\log L_{[\text{OIII}]}^b$ [erg/s]	$r_e^c$ [kpc]
HE 0952–1552	$43.98 \pm 0.09$	$41.88 \pm 0.10$	$3.4 \pm 0.1$
HE 1019–1414	$43.40 \pm 0.11$	$41.94 \pm 0.11$	$1.9 \pm 0.1$
HE 1029–1401	$44.94 \pm 0.09$	$42.39 \pm 0.11$	$4.5 \pm 0.1$
HE 1110–1910	$44.05 \pm 0.10$	$41.66 \pm 0.11$	$3.2 \pm 1.1$
HE 1228–1637	$44.08 \pm 0.10$	$41.67 \pm 0.14$	$<1.8$
HE 1237–2252	$43.44 \pm 0.11$	$41.22 \pm 0.13$	$2.4 \pm 0.3$
HE 1239–2426	$43.81 \pm 0.10$	$41.20 \pm 0.11$	$1.9 \pm 0.1$
HE 1254–0934	$44.68 \pm 0.11$	$42.53 \pm 0.12$	$3.8 \pm 0.1$
HE 1300–1325	$43.46 \pm 0.09$	$41.23 \pm 0.09$	$<1.4$
HE 1310–1051	$43.55 \pm 0.10$	$41.66 \pm 0.14$	$<1.9$
HE 1338–1423	$43.73 \pm 0.10$	$42.00 \pm 0.13$	$2.0 \pm 0.0$
HE 1405–1545	$44.22 \pm 0.11$	$42.03 \pm 0.12$	$4.6 \pm 0.1$
HE 1416–1256	$44.13 \pm 0.12$	$42.85 \pm 0.11$	$5.6 \pm 0.5$

<sup>a</sup>QSO continuum luminosity at 5100 after removing the contribution from the host galaxy. <sup>b</sup>Integrated [OIII] luminosity from the unresolved QSO and extended ENLR. <sup>c</sup>[OIII] luminosity-weighted effective ENLR radius excluding the HII-like regions. Upper limits are derived for those objects which do not show an ENLR and represent the shortest distance to an HII-like region.

## 4.6 Gas-phase oxygen abundances

### 4.6.1 HII-like regions

Oxygen abundances of HII regions can be estimated from various empirically calibrated emission-line ratios of strong lines, the so-called strong-line method. Commonly used strong-line calibrations are the  $R_{23}$  index (e.g. Pagel et al. 1979; Edmunds & Pagel 1984; Dopita & Evans 1986; Pilyugin 2001; Pilyugin & Thuan 2005), the N2 index (Storchi-Bergmann, Calzetti & Kinney 1994; Denicoló, Terlevich & Terlevich 2002; Pettini & Pagel 2004) and the O3N2 index (Alloin et al. 1979; Pettini & Pagel 2004). Since the [OII]  $\lambda 3727$  is not covered within the wavelength range of our observations, we could not compute the  $R_{23}$  index. The N2 index is based only on the [NII] and H $\alpha$  lines, but is not very sensitive at high metallicities. Therefore, we used the O3N2 index and the linear calibration derived by Pettini & Pagel (2004) (hereafter PP04) as the most suited oxygen abundance calibrator for our available set of emission lines. The systematic uncertainty of  $\sim 0.15$  dex for this calibration is significantly larger than other methods because the ionization parameter cannot be taken into account. On the other hand, it has the advantage of being single-valued in contrast to the  $R_{23}$  index.

All estimated oxygen abundances need to be used with care as every method has its strengths and weaknesses, which are still heavily debated in the literature (e.g. Pagel, Edmunds & Smith 1980; Kennicutt & Garnett 1996; Kewley & Dopita 2002; Pérez-Montero & Díaz 2005; Kewley & Ellison 2008; López-Sánchez et al. 2012). Comparing oxygen abundances obtained with different calibrations reveals large systematic offsets up to 0.5 dex in  $\log(\text{O}/\text{H})$  (Liang et al. 2006; Kewley & Ellison 2008). Transformations between the different calibrations, in particular with the O3N2 index, were determined by Kewley & Ellison (2008). We scaled our inferred PP04 oxygen abundances to the calibration adopted by Tremonti et al. (2004) (hereafter, T04) as a reference using the correction function from Kewley & Ellison (2008). This allows us to compare the oxygen abundances of our QSO host galaxies with respect to the stellar mass-metallicity relation as presented

by T04 for star forming SDSS galaxies. Our approach is valid here, because we are only interested in a relative comparison between the oxygen abundances rather than in its absolute value.

### 4.6.2 AGN-ionized regions

Gas-phase element abundance calibrations for the AGN photoionized ENLR are largely unexplored. Currently, only photoionization models can be used to quantitatively estimate the element abundance of the gas in that case. Storchi-Bergmann et al. (1998) computed the oxygen abundances for an artificial grid of line ratios with the photoionization code CLOUDY using an empirical AGN spectrum for the ionizing source. They estimated a calibration based on the [OIII]  $\lambda\lambda 4960, 5007/\text{H}\beta$  and [NII]  $\lambda\lambda 6548, 6583/\text{H}\alpha$  line ratios by fitting a two-dimensional polynomial of second-order to the resulting grid of oxygen abundances with an additional dependence on the electron density ( $n_e$ ).

For a rough estimate of  $n_e$ , we employed the density-sensitive [SII]  $\lambda\lambda 6716, 6731$  doublet line ratio (e.g. Osterbrock & Ferland 2006). The inferred electron densities in the ENLR range between  $100\text{--}300\text{ cm}^{-3}$ , so that we adopted an electron density of  $n_e = 200\text{ cm}^{-3}$  for the oxygen abundance calibration of Storchi-Bergmann et al. (1998). We emphasize that a change of  $n_e$  by a factor of 2 would alter the oxygen abundance by 0.03 dex only.

Since the calibration of Storchi-Bergmann et al. (1998) was based on CLOUDY photoionization models, the oxygen abundances are comparable to the ones based on the T04 calibration for star-forming galaxies. One remaining systematic uncertainty is introduced by the choice of the adopted AGN ionizing spectrum. Storchi-Bergmann et al. (1998) found that oxygen abundances are up to 0.5 dex larger when the AGN spectrum is approximated by a pure power-law function. Here, we empirically tied the ENLR oxygen abundances with those of HII-like regions in the host galaxies of HE 0952–1552 and HE 1405–1545 in which both could be determined at a similar distance from the galaxy centre. We found a systematic difference of  $\approx 0.2$  dex between the estimate oxygen abundances of the ENLR and the HII-like regions and corrected then ENLR oxygen abundances accordingly.

## 5 RESULTS AND DISCUSSION

### 5.1 The size–luminosity relation for the ENLR

In Husemann et al. (2013b), we studied the size of the ENLR for a sample of luminous QSOs. The covered luminosity range of that sample alone was too narrow to reliably constrain the slope of a presumed ENLR size–luminosity relation. With the sample of type 1 QSOs presented in this work, we significantly extend the range towards lower luminosities allowing us to investigate this relation in more detail. Additionally, VIMOS IFU data for five Seyfert 1 galaxies (Fairall 265, Fairall 51, Mrk 915, NGC 3783, NGC 4593) are available (Kupko et al. in prep.), which further complement our sample. In Fig. 7, we compare the ENLR sizes with the integrated [OIII] luminosities (left panel) and the QSO continuum luminosities at  $5100\text{Å}$  (right panel), which are both frequently used proxies for the intrinsic bolometric luminosities of AGN.

A clear correlation between the ENLR sizes and the corresponding luminosities is evident in both cases. For a proper statistical analysis of these correlations we took the censored data points into account. The Astronomy Survival Analysis package (ASURV, Lavalley, Isobe & Feigelson 1992) was specifically developed for

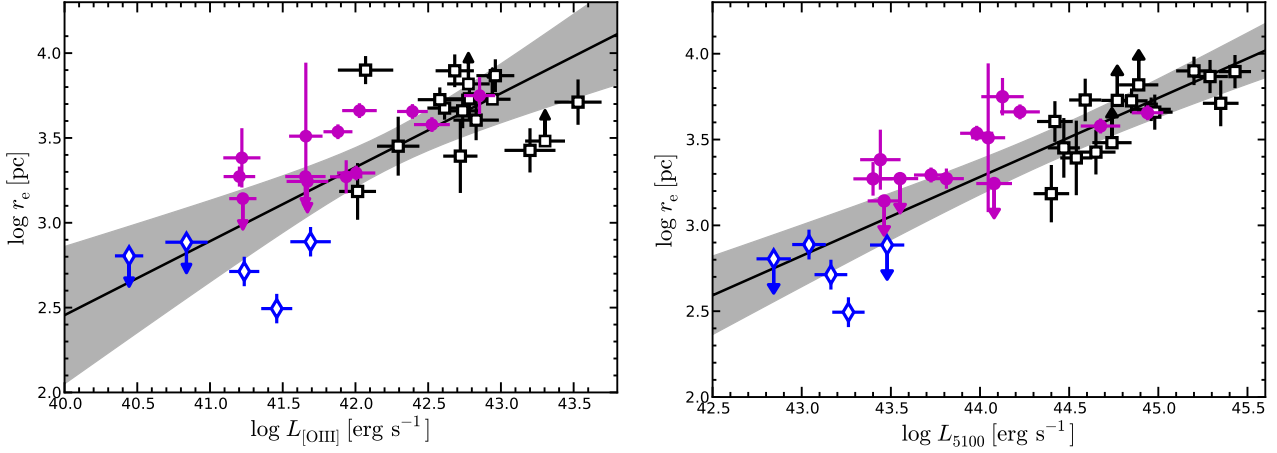


**Figure 7.** ENLR size as a function of integrated [OIII] luminosity (left panel) or AGN continuum luminosity at 5100Å (right panel). The data from this sample are shown as filled circles in magenta colour. Additional measurements for luminous type-1 QSOs (Husemann et al. 2013b) and from 5 Seyfert 1 galaxies (Kupko et al. in prep.) are shown as black open squares and blue open diamonds, respectively. Arrows indicate upper limits on the ENLR size. The solid line represent the linear relations inferred from the Buckley-James method. The shaded areas correspond to the  $1\sigma$  error of the relation which we derived with a bootstrap approach.

this task and incorporates several statistical methods to deal with bi-variate censored data (Isobe, Feigelson & Nelson 1986). We computed the generalized Spearman’s Rho correlation coefficient and found a significant correlation between the ENLR size and the AGN continuum luminosity with a coefficient of 0.87 at a confidence level greater than 99.99 per cent. A somewhat smaller correlation coefficient of 0.76 was computed for the correlation with the integrated [OIII] luminosity at a confidence level of 99.99 per cent.

The ENLR size-luminosity relation has usually been approximated by a power law function,  $\log(R_{\text{ENLR}}) = \alpha \log(L_{\text{AGN}}) + R_0$ . Here, we use the effective ENLR radius ( $r_e$ ) as described in Sec. 4.5 for the ENLR size ( $R_{\text{ENLR}}$ ) and the integrated [OIII] luminosity ( $L_{[\text{OIII}]}$ ) and the AGN continuum luminosity at 5100Å ( $L_{5100}$ ) as two independent estimates for the intrinsic AGN luminosity ( $L_{\text{AGN}}$ ). A linear regression analysis taking into account censored data points is the Buckley-James method (Buckley & James 1979) which yields the following parameters

$$\log r_e = (0.44 \pm 0.06) \times \log L_{[\text{OIII}]} - (14.98 \pm 2.47), \quad (2)$$

$$\log r_e = (0.46 \pm 0.04) \times \log L_{5100} - (16.95 \pm 1.61). \quad (3)$$

We estimate the errors on the parameters with a bootstrap approach. We repeat the regression analysis for 200 samples containing only 80% of the objects which we randomly selected from the parent sample. In addition, we vary the data points within the corresponding normal distribution given by their  $1\sigma$  uncertainties.

The correlation between the ENLR size and the AGN continuum luminosity is tighter than the correlation with [OIII] luminosity as reported in Husemann et al. (2013b) and confirmed for this expanded sample. Our IFU dataset now contains more than 40 type 1 AGN and covers 3 orders of magnitude in luminosity, which shows that the relation is consistent with a slope of  $\alpha \sim 0.5$  within the errors. It was already discussed in Greene et al. (2011) and Husemann et al. (2013b) that the absolute zero-point  $R_0$  of this relation is difficult to compare among the previous studies when different depth-dependent definitions for the ENLR size are used. In the following, we restrict the discussion to the slope  $\alpha$  of the relation.

A slope of  $\alpha \sim 0.5$  for the ENLR size-luminosity relation

was initially reported by Bennert et al. (2002) and can be easiest explained by a constant ionization parameter for gas clouds across the ENLR. This has also been the favoured scenario for the BLR size-luminosity relation (e.g. Bentz et al. 2009). Because the scales of the ENLR are orders of magnitude larger than the BLR, it is still unclear whether a constant ionization parameter can be a realistic scenario on host galaxy scales. A different slope of the relation would indicate that other physical conditions and processes play a key role. A flatter slope of  $\alpha = 0.33 \pm 0.04$  was inferred by Schmitt et al. (2003) from a sample of 60 nearby Seyfert galaxies observed with *HST*. However, the *HST* narrow-band images used by Bennert et al. (2002) and Schmitt et al. (2003) were much shallower compared to current ground-based observations. Moreover, it was not possible to distinguish between [OIII] emission from the ENLR and HII-like regions.

An even flatter slope was recently presented by Greene et al. (2011) and Liu et al. (2013) of  $\alpha = 0.22 \pm 0.04$  and  $\alpha = 0.25 \pm 0.02$ , respectively. They used deep ground-based optical long-slit and IFU spectroscopy to map the ENLR of luminous type 2 QSO at redshift  $0.1 < z < 0.5$  combined with literature data of low-redshift Seyfert 2 galaxies. Greene et al. (2011) proposed a model where the ENLR is matter-bounded, i. e. the emission is limited by the gas density rather than the density of ionizing AGN photons. However, their sample is quite heterogeneous and collected from different samples in the literature that used different observing techniques. Recently, Hainline et al. (2013) added 8 type 2 AGN to the sample and confirmed the flat relation between the ENLR size and [OIII] luminosity. Interestingly, they find a slope of  $\alpha \sim 0.5$  instead by using the  $8\mu\text{m}$  luminosity as an alternative AGN luminosity indicator, which is consistent again with the slope we report here.

From our homogeneous sample of genuine type 1 QSOs we infer robust upper limits for ENLR sizes for the lower luminosity QSOs where the ionization is dominated by HII-like regions close to the QSO at our resolution limit. Those limits are consistent with detected ENLRs at similar luminosities and significantly smaller than assumed for the type 2 Seyfert galaxies inferred from the Fraquelli, Storchi-Bergmann & Levenson sample. On the other hand, it still remains open how undetected ENLRs around some

luminous type 1 QSOs, presented in Husemann et al. (2008) and Husemann et al. (2013b), fit into a common ENLR size-luminosity relation for all AGN and what role radio jets have on the ENLR properties (e.g. Wu 2009; Husemann et al. 2013b; Mullaney et al. 2013).

## 5.2 Ongoing star formation in QSO host galaxies

### 5.2.1 $H\alpha$ -based star formation rates from the IFU data

We used the integrated  $H\alpha$  luminosity ( $L_{H\alpha}$ ) of HII-like regions in our QSO host galaxies to estimate the current SFR, adopting the calibration of Kennicutt (1998),

$$\frac{\text{SFR}}{M_{\odot}\text{yr}^{-1}} = \frac{L_{H\alpha}}{1.26 \times 10^{41} \text{ erg s}^{-1}}. \quad (4)$$

The effect of reddening was estimated for the individual HII-like regions in the host galaxies from the observed  $H\alpha/H\beta$  Balmer decrement in comparison to the theoretically expected value of 2.86 at  $T_e = 10\,000\text{K}$  assuming case B recombination (Osterbrock & Ferland 2006). We computed the  $V$  band attenuation ( $A_V$ ) from the Balmer decrement adopting a standard Milky way attenuation law (Cardelli, Clayton & Mathis 1989) and  $R_V = 3.1$ . The variance weighted mean attenuation of all individual regions of the host galaxy is included in Table 5 to allow a global comparison of the dust attenuation between the different host galaxies and companions. We find that the attenuation is typically modest with  $A_V < 1.7$  mag except for a very high attenuation of  $A_V \sim 4.1$  mag in the close companion/second nucleus of the ongoing major-merger system HE 1254–0934. A significant difference exists between the bulge and disc-dominated systems in general. The mean attenuation for the bulge-dominated hosts ( $\langle A_V \rangle = 0.9$  mag) is on average only 2/3 that for the disc-dominated hosts ( $\langle A_V \rangle = 1.4$  mag) in our sample.

We measure the total  $H\alpha$  fluxes by summing up all the  $H\alpha$  flux from HII-like regions (including the intermediate ones) for each host galaxy. From the attenuation-corrected  $H\alpha$  luminosities, we estimate the SFRs with Eq. 4 and compute the specific SFRs ( $\text{SSFR} \equiv \text{SFR } M_{*}^{-1}$ ) with the SED-based estimates of  $M_{*}$  for our host galaxies. All values are listed in Table 5 including the systematic uncertainties and offsets of the QSO host-deblending process as determined in Appendix A from extensive simulations. For HE 1335–0847 we obtain the SFR from the  $H\beta$  luminosity, adopting the mean reddening of  $A_V = 0.9$  mag for bulge-dominated systems because the spectral region containing the  $H\alpha$  line was not observed for this object. Similarly, we also adopt the mean reddening for HE 1110–1910, given that the Balmer decrement suffered from an unacceptably large uncertainty in  $H\beta$  flux. For all the other QSOs that are exclusively dominated by emission from the ENLR, we constrain robust upper limits on the SFR by integrating the entire  $H\alpha$  emission which represents the maximum contribution of HII-like emission to the ENLR. Exceptions are HE 1201–2409 and HE 1434–1600 which are not fully covered within the instrument FoV.

### 5.2.2 Comparison with IR and radio-based star formation rates

The  $H\alpha$ -based SFRs are affected by dust attenuation and systematic uncertainties of the QSO-host deblending at our seeing-limited spatial resolution. Thus, we compare them with SFRs inferred from alternative IR and radio tracer. It was shown that the extinction-corrected  $H\alpha$  luminosity agrees very well with the IR (Kewley et al.

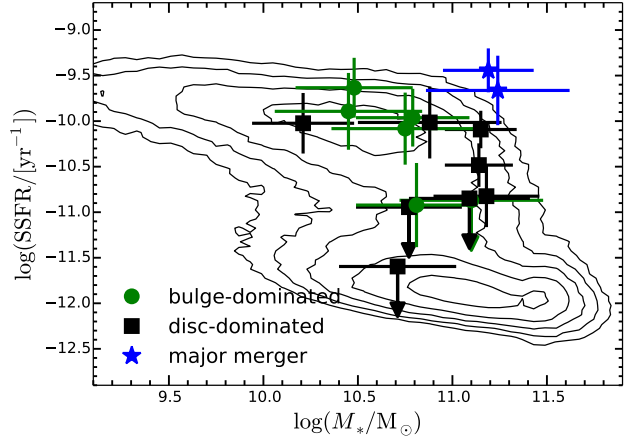


**Figure 8.** Specific SFR against the total stellar mass of the QSO host galaxies. The SFRs are estimated from the integrated attenuation-corrected  $H\alpha$  luminosity of HII-like region (filled coloured symbols) and the 60+100 $\mu\text{m}$  FIR luminosity (open grey symbols) using the calibrations of Kennicutt (1998) and Bell (2003), respectively. Upper limits for the  $H\alpha$  luminosity are determined for cases where the ENLR dominates the emission across the host galaxy. They are based on the integrated  $H\alpha$  luminosity as the maximum possible contribution from any underlying HII-like regions. Despite the numerous upper limits, the IR luminosity appears to be systematically contaminated by AGN emission and the  $H\alpha$  luminosity provides a more reliable SFR indicator for these QSOs. For comparison, the distribution in SSFR of galaxies in the SDSS MPA/JHU galaxy catalogue (Brinchmann et al. 2004) is shown as contours in logarithmic scaling.

2002; Domínguez Sánchez et al. 2012) and radio luminosity (e.g. Bell 2003) in normal star-forming galaxies and therefore leads to consistent SFRs. For luminous AGN this is not correct, because jets can contribute to the radio luminosity and the AGN-heated dust contribute to the 60 $\mu\text{m}$  and 100 $\mu\text{m}$  accessible with IRAS. The IR and radio luminosities can therefore only provide upper limits on the SFR and need to be considered with care.

Here we adopt the calibrations of Bell (2003) to estimate the SFR from the IR and radio luminosities as follows:

For  $L_{1.4\text{GHz}} > 6.4 \times 10^{21} \text{ W Hz}^{-1}$

$$\text{SFR}_{\text{radio}} = 5.52 \times 10^{-22} L_{1.4\text{GHz}} \quad (5)$$

and for  $L_{1.4\text{GHz}} \leq 6.4 \times 10^{21} \text{ W Hz}^{-1}$ :

$$\text{SFR}_{\text{radio}} = \frac{5.52 \times 10^{-22}}{0.1 + 0.9(L_{1.4\text{GHz}}/6.4 \times 10^{21} \text{ W Hz}^{-1})} L_{1.4\text{GHz}} \quad (6)$$

Similarly, for  $L_{\text{IR}} > 10^{11} L_{\odot}$

$$\text{SFR}_{\text{IR}} = 1.57 \times 10^{-10} L_{\text{IR}} \left( 1 + \sqrt{\frac{10^9}{L_{\text{IR}}}} \right) \quad (7)$$

and for  $L_{\text{IR}} \leq 10^{11} L_{\odot}$

$$\text{SFR}_{\text{IR}} = 1.17 \times 10^{-10} L_{\text{IR}} \left( 1 + \sqrt{\frac{10^9}{L_{\text{IR}}}} \right) \quad (8)$$

$L_{\text{IR}}$  is the total IR luminosity between 8–1000 $\mu\text{m}$ . We assume that the total IR flux is a factor of  $\sim 1.75$  higher (Calzetti et al. 2000) than the FIR flux between 40–120 $\mu\text{m}$  which we compute from the IRAS fluxes given in Janskys as  $\text{FIR} = 1.26 \times 10^{-14} (2.58\text{F}_{60\mu\text{m}} + \text{F}_{100\mu\text{m}}) \text{ W m}^{-2}$  (Helou et al. 1988).

The IRAS IR luminosity or upper limits and NVSS radio luminosity often correspond to SFRs for our AGN that are several



**Table 5.** Integrated properties of HII-like regions

Object <sup>a</sup>	$f(\text{H}\alpha)^c$ [ $10^{-16} \text{ erg cm}^{-2} \text{ s}^{-1}$ ]	$f_{\text{cor}}(\text{H}\alpha)^d$ [ $10^{-16} \text{ erg cm}^{-2} \text{ s}^{-1}$ ]	$A_V^e$ [mag]	$L_{\text{cor}}(\text{H}\alpha)^f$ [ $\text{erg s}^{-1}$ ]	$\text{SFR}_{\text{H}\alpha}^g$	$\text{SFR}_{\text{FIR}}^h$ [ $\text{M}_{\odot} \text{ yr}^{-1}$ ]	$\text{SFR}_{1.4\text{GHz}}^i$	$\log \text{sSFR}^j$ [ $\text{yr}^{-1}$ ]
HE 0952–1552	16.2 ± 1.3	57 ± 11	1.7 ± 0.1	41.23 ± 0.09	2.3 ± 1.0	<45.1	93.8	−10.8 ± 0.3
HE 1019–1414 <sup>b</sup>	< 23.7	< 58	...	< 40.93	< 0.7	<20.5	39.9	< −10.9
HE 1029–1401 <sup>b</sup>	< 74.9	< 118	...	< 41.33	< 1.7	<25.8	149.2	< −10.9
HE 1043–1346	144.7 ± 16.1	987 ± 472	1.2 ± 0.1	42.04 ± 0.27	7.3 ± 3.4	25.7	<7.9	−10.0 ± 0.4
HE 1110–1910	10.0 ± 1.8	16 ± 3	1.1 ± 0.8	40.70 ± 0.08	0.8 ± 0.4	<44.8	<22.1	−10.9 ± 0.5
HE 1228–1637	176.2 ± 14.3	377 ± 114	0.8 ± 0.2	42.01 ± 0.15	6.7 ± 2.5	<38.9	<19.2	−10.0 ± 0.3
HE 1237–2252	58.1 ± 3.0	230 ± 158	0.8 ± 0.1	41.76 ± 0.35	4.5 ± 2.7	45.6	<16.6	−10.5 ± 0.2
HE 1239–2426	196.9 ± 7.9	920 ± 144	1.5 ± 0.1	42.18 ± 0.07	11.4 ± 4.3	32.7	22.0	−10.1 ± 0.2
HE 1254–0934	79.4 ± 8.6	1698 ± 227	4.1 ± 0.1	42.94 ± 0.06	55.9 ± 8.7	161.4	432.6	−9.4 ± 0.2
HE 1300–1325	354.8 ± 17.1	1352 ± 110	1.4 ± 0.1	41.84 ± 0.04	4.7 ± 0.5	8.9	<3.6	−10.1 ± 0.4
HE 1315–1028 <sup>b</sup>	< 2.8	< 7	...	< 40.21	< 0.1	<34.8	<17.1	< −11.6
HE 1310–1051	134.9 ± 6.7	594 ± 73	1.7 ± 0.1	41.21 ± 0.05	1.5 ± 0.5	<3.2	<1.9	−10.0 ± 0.3
HE 1335–0847	120.2 ± 39.8	189 ± 60	...	41.48 ± 0.16	7.0 ± 3.1	<22.7	<11.1	−9.6 ± 0.3
HE 1338–1423 <sup>b</sup>	< 229.8	< 567	...	< 41.34	< 1.7	<4.6	10.7	< −10.8
HE 1405–1545	153.5 ± 7.9	444 ± 39	1.3 ± 0.1	42.68 ± 0.04	37.7 ± 8.6	<149.5	<73.1	−9.7 ± 0.4
HE 1416–1256	61.9 ± 11.5	62 ± 12	< 0.5	41.44 ± 0.09	3.6 ± 1.8	<61.1	49.5	−9.9 ± 0.4

<sup>a</sup> Companion galaxies are denoted with a (c) behind the name of the corresponding QSO. <sup>b</sup> Galaxies for which the extended emission is dominated by the ENLR. Integrating the H $\alpha$  flux of the ENLR provides a firm upper limit on the possible contribution of HII-like regions. We use the mean attenuation for each morphological type to roughly take dust extinction effects into account for the upper limit. <sup>c</sup> Integrated H $\alpha$  flux of all HII-like and intermediate regions of a galaxy. <sup>d</sup> Attenuation-corrected H $\alpha$  flux. <sup>e</sup> Mean attenuation of all specific regions of a galaxy taking into account the individual uncertainties as weights. <sup>f</sup> Attenuation-corrected H $\alpha$  luminosity. <sup>g</sup> SFR estimated from the attenuation-corrected H $\alpha$  luminosity following Kennicutt (1998). Systematic offsets and uncertainties based on the results from extensive simulations (Sect. A) are already taken into account in the reported SFRs. <sup>h</sup> H $\alpha$ -based specific SFR are computed with the SED-based stellar masses (see Table 1).

factors higher than the ones derived from the H $\alpha$  luminosity (see Fig. 8). The radio-based SFRs are also often lower than the IR-based ones which indicates that the AGN contribution to the FIR is significant despite the fact that the radio flux itself is contaminated by additional flux from jets. Thus, the spatially resolved extinction-corrected H $\alpha$  luminosity appears to be the most reliable SFR tracer for our AGN host galaxies. It also offers the highest spatial resolution compared to IR and radio surveys.

### 5.2.3 Discussion of specific star formation rates

Although the attenuation correction significantly increases the uncertainty for the estimated SFRs, the SFRs of our AGN host galaxies typically range between  $1 \text{ M}_{\odot} \text{ yr}^{-1}$  and  $10 \text{ M}_{\odot} \text{ yr}^{-1}$ . However, the absolute SFR is well correlated with stellar mass, so that the SSFR is nearly constant for the bulk population of disc-dominated galaxies. We compare the SSFR as a function of stellar mass for our QSO host galaxies in Fig. 8 with the overall distribution of star forming galaxies within SDSS presented by Brinchmann et al. (2004). We find that the majority of our disc-dominated system shows signatures of ongoing star formation and are consistent with the main sequence of star-forming galaxies. Three of them have upper limits placing them below the main sequence of which HE 1315–1028 is an extreme case. This galaxy does not show any detectable emission of ionized gas except of an ENLR at its outskirts and therefore is very likely a gas poor system compared to the rest. The bulge-dominated QSO hosts appear to have diverse properties. Two bulge-dominated QSO hosts, HE 1228–1637 and HE 1300–1325 are located on the main sequence, whereas HE 1335–0847 and HE 1110–1910 display roughly an order of magnitude lower SSFRs compared to the main sequence. Still they are certainly not consistent with the SSFR expected for bulge-

dominated galaxies on the red sequence, which is unclear for HE 1029–1401 as its bright and extended ENLR makes it impossible to infer the contribution from star formation to the H $\alpha$  luminosity. On the other hand, the SSFR is significantly enhanced for the two ongoing major mergers in our sample. To summarize, we find that 2 out of 16 QSO hosts (13 per cent) exhibit enhanced star formation, 8 of 16 QSO hosts (50 per cent) are consistent with the main sequence of star-forming galaxies, and 6 of 16 QSO hosts (38 per cent) show at least intermediate levels of star formation between the main sequence and the quiescent red-sequence or even lower.

Previous attempts to characterize the SFR of luminous QSOs used the [OII] line in the integrated spectrum as a SFR indicator. For example, Ho (2005) and Kim, Ho & Im (2006) found that most of the [OII] emission in a sample PG and SDSS type-1 QSO originates mainly from the NLR with a low SFR and therefore conclude that star formation is generally suppressed in QSO host galaxies. On the contrary, Silverman et al. (2009) used the same technique to infer the SFR for a large X-ray selected sample of AGN and found that their host galaxies exhibit on average a higher SFR compared to normal galaxies at a given stellar mass. Such enhanced levels of star formation are also found in studies that used the mid- and far-infrared wavelength to disentangle the relative contribution of AGN and star formation (e.g. Schweitzer et al. 2006; Netzer et al. 2007; Lacy et al. 2007). They additionally report that the SFR is correlated with the QSO luminosity.

Only the ongoing major mergers in our sample exhibit enhanced SSFRs, but for a large fraction of the undisturbed QSO host galaxies the SSFR is consistent with those of inactive galaxies. This picture is in agreement with recent results from far-infrared studies of AGN host galaxies based on Herschel data (Santini et al. 2012; Rosario et al. 2012). On the other hand, we also find that six

QSO hosts have intermediate or very low SSFRs based on the  $H\alpha$  luminosity independent of their morphological type. Either the star formation efficiency in the galaxy are directly reduced by the presence of the AGN or the intrinsic gas content is lower compared to the other galaxies on galaxy-wide scales. This is something we cannot address with this dataset alone as the information on the molecular gas content is missing. HE 1310–1051 and HE 1338–1423 were observed with the IRAM 30m telescope in CO emission so far (Bertram et al. 2007), but only upper limits on the molecular gas masses of around  $< 0.5 \times 10^9 M_\odot$  could be inferred. The reasons for the non-detection of clear HII-like regions therefore remain open. However, AGN feedback generally cannot be present, or must be significantly delayed after the onset of the QSO phase, considering the large fraction of galaxies with normal or enhanced levels of star formation. The construction of control samples of inactive galaxies with matching galaxy properties is therefore crucial to infer the immediate impact of AGN.

### 5.3 Oxygen abundances distribution in QSO host galaxies: Signature for internal processes or external gas supply?

We construct the gas-phase metallicity gradients for six of our QSO host galaxies with sufficient radial coverage (Fig. 9). The galactocentric distances are normalized by the effective radius ( $R_e$ ) of the corresponding host galaxies to put them on a comparable scale. For undisturbed inactive late-type galaxies, negative gas-phase metallicity gradients were recovered in numerous spectroscopic studies of the HII regions (e.g. McCall, Rybski & Shields 1985; Vila-Costas & Edmunds 1992; Zaritsky, Kennicutt & Huchra 1994; Henry & Worthey 1999; Kennicutt, Bresolin & Garnett 2003; Magrini et al. 2007; Viironen et al. 2007; Sánchez et al. 2012b). A reference for a statistically robust oxygen abundance gradient for disc-dominated galaxies was recently provided by Sánchez et al. (2012b) based on data from the PINGS (Rosales-Ortega et al. 2012) and the CALIFA survey (Sánchez et al. 2012a), which we indicated as a dashed line in Fig. 9 for comparison.

These few QSO host galaxies with recovered gas-phase metallicity gradients do not represent a statistically meaningful sample. Nevertheless, we note that the late-stage merger HE 1405–1545 exhibits a strong positive gradient. This is in contrast to the disc-dominated galaxies which are statistically consistent with the expected negative gradient despite a global metallicity offset. The results are less clear for the two bulge-dominated QSO host galaxies. Although HE 1300–1325 appears to have at least a similar slope than the disc-dominated ones, the gas-phase metallicity remains constant up to  $1.5 R_e$  and exhibits a pronounced drop in the oxygen abundance at this location which mimics a global negative gradient. The galaxy is in a very early interaction phase with its major companion and the gradient is a superposition of an inner rotating gas disc and a kinematically detached tidal arm that extends out to  $3 R_e$  radii. On the other hand, the abundance gradient in the bulge-dominated galaxy HE 1029–1401 appears to be flat as already discussed in Husemann et al. (2010). A caveat could be that it is solely based on the oxygen abundance measurements from the ENLR which might be prone to other systematic effects, i. e. QSO luminosity, as pointed out by Stern & Laor (2013).

To take better advantage of the sample size, we measure the oxygen abundance at  $\sim 1 R_e$  (Table 6) as the average of abundances between  $0.75 R_e < R < 1.25 R_e$ . This measurement can be done for the majority of our objects. In the case of HE 0952–1552, HE 1029–1401, HE 1043–1346, HE 1239–2426, and HE 1300–1325 the radial distribution is suf-

**Table 6.** Gas-phase oxygen abundances of QSO host galaxies

Object	$12 + \log(\text{O}/\text{H})_{\text{T04}}^a$	Indicator <sup>b</sup> .
HE 0952–1552	$(8.75/8.91) \pm 0.03(\pm 0.07)$	NLR
HE 1019–1414	$(8.95/9.10) \pm 0.19(\pm 0.08)$	NLR
HE 1029–1401	$(8.81/8.96) \pm 0.04(\pm 0.05)$	NLR
HE 1043–1346	$(9.08/9.23) \pm 0.06(\pm 0.04)$	O3N2
HE 1228–1637	$(8.83/8.98) \pm 0.10(\pm 0.04)$	O3N2
HE 1237–2252	$(8.98/9.13) \pm 0.08(\pm 0.05)$	O3N2
HE 1239–2426	$(8.96/9.11) \pm 0.03(\pm 0.05)$	O3N2
HE 1300–1325	$(8.75/8.90) \pm 0.04(\pm 0.02)$	O3N2
HE 1310–1051	$(8.73/8.88) \pm 0.05(\pm 0.04)$	O3N2
HE 1405–1545	$(8.73/8.88) \pm 0.04(\pm 0.05)$	O3N2
HE 1416–1256	$(8.59/8.74) \pm 0.05(\pm 0.13)$	O3N2
HE 1434–1600	$(8.73/8.88) \pm 0.04(\pm 0.08)$	NLR

<sup>a</sup>Two metallicities are given. The first one is measured at  $1 R_e$  of the host galaxy from the data and the second is an extrapolated one towards the galaxy center assuming a slope of radius-metallicity as reported by Sánchez et al. (2012b). All metallicities and the radius-metallicity slope are converted to the Tremonti et al. (2004) oxygen abundance scale using the conversion of Kewley & Ellison (2008). The measurement errors and the systematic errors are provided. The systematic errors are based on the extensive simulation of the QSO-host deblending process presented in Sect. A.

<sup>b</sup>Metallicities are either inferred using the O3N2 index of Pettini & Pagel (2004) for HII regions or using the calibration of Storch-Bergmann et al. (1998) for the ENLR.

ficient to estimate a linear relation, which we evaluate at  $1 R_e$  to provide a consistent measurement with respect to the other objects. Assuming the slope of the radius-metallicity relation from Sánchez et al. (2012b), we extrapolated the oxygen abundance at  $1 R_e$  towards the centre of the host galaxies.

We compare the extrapolated central oxygen abundances against the stellar masses determined from the broad-band SED of the galaxies in Fig. 10. Our disc-dominated QSO host galaxies follow the mass-metallicity relation of galaxies (Tremonti et al. 2004) whereas the bulge-dominated ones have systematically lower oxygen abundances at a given stellar mass. Interestingly, the bulge-dominated host HE 1416–1256 and the major merger HE 1405–1545 exhibit particularly low oxygen abundances that are well below the mass-metallicity relation. The significance of our result might be reduced by the systematic uncertainties of 0.15 dex for the strong-line oxygen abundance calibrators. However, such uncertainties must *randomly* affect the overall sample and not selectively affect only a certain morphological type, except when there is a physical reason, e. g. when the ionization parameter for the HII-like regions depends on the host morphology.

Given that the general mass-metallicity relation is almost flat in the high-mass regime, it is ruled out that the lower abundance can be explained only with a strong offset in stellar mass. It would require the stellar masses to be overestimated by an order of magnitude to be on the relation, which is beyond the uncertainties of our measurements and cannot be explained by the doubling of mass during a 1:1 merger. However, it is likely that a dilution in oxygen abundance and the immediate mass increase of the merger act together in this respect. The measurement of the effective radius can also be affected by systematic uncertainties. In particular, for bulge-dominated systems the effective radius can be systematically underestimated during the QSO-host deblending caused by flux transfer from the QSO to the host galaxy profile. This would reduce the distance of our HII-like regions with respect to the effective radius and

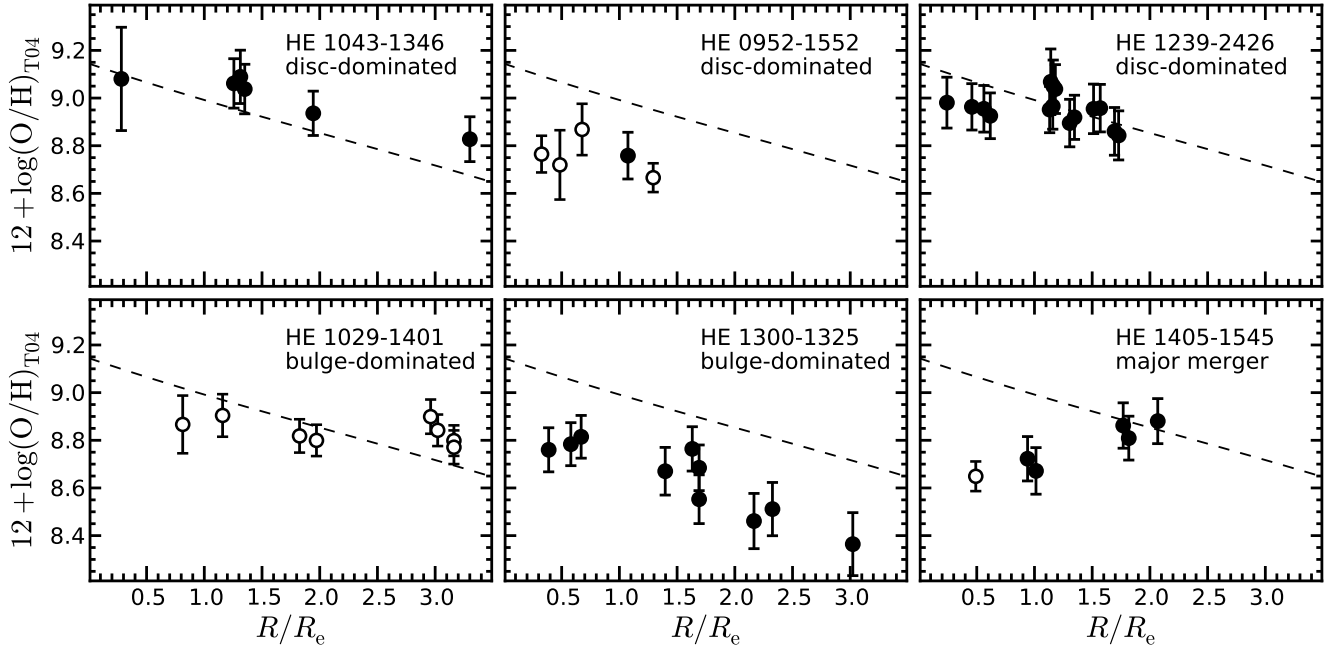


**Figure 9.** Oxygen abundance as a function of effective radius for the six QSO host galaxies with sufficient radial coverage. Filled symbols denote abundance estimates based on HII-like regions using the O3N2 index from Pettini & Pagel (2004), whereas open symbols refer to abundances based on the NLR adopting the calibration of Storchi-Bergmann et al. (1998). The radial oxygen abundance gradient derived from 38 face-on disc-dominated galaxies (Sánchez et al. 2012b) is shown as the dashed line for comparison. All abundances are rescaled to match the Tremonti et al. calibration applying the correction derived by Kewley & Ellison (2008).

lower the extrapolated central oxygen abundance even further compared to the disc-dominated system in favour of our conclusions.

One difficulty to interpret our results is that the gas-phase metallicities of inactive elliptical and bulge-dominated galaxies are not well explored. It is known that more than 60 per cent of the elliptical galaxies display detectable emission lines of warm ionized gas (e.g. Trinchieri & di Serego Alighieri 1991; Goudfrooij et al. 1994; Macchetto et al. 1996; Sarzi et al. 2006). The gas is often concentrated at the nucleus with LINER-like emission which appears to be predominately ionized by post-AGB stars or a low-luminosity AGN rather than ongoing star formation. Metallicities of elliptical galaxies were mainly obtained from their hot gas phase and their stellar population (e.g. Trager et al. 2000). Only a few recent studies tried to infer the metallicity of the warm-ionized gas, concentrating on the galaxy centre. Annibali et al. (2010) found that the gas-phase oxygen abundances in a sample of 65 inactive bulge-dominated galaxies were systematically lower than the corresponding stellar abundances. They attributed this discrepancy either to a systematic mismatch between the gas-phase and stellar abundance calibrations or to the accretion of external gas, likely via minor mergers. Additional evidence for the external origin of the gas in a large fraction of bulge-dominated galaxies comes from the misaligned kinematics of ionized gas (e.g. Caon, Macchetto & Pastoriza 2000; Sarzi et al. 2006) and molecular gas (Davis et al. 2011) with respect to the stars. Contrarily, Athey & Bregman (2009) argued that the solar metallicity gas in elliptical galaxies is unlikely to be accreted from the environment, and they favoured mass loss from AGB stars as the origin of the gas.

It is therefore intriguing to find that the bulge-dominated QSO host galaxies and the systems with ongoing interactions are offset from the mass-metallicity relation. While the assumed radius-metallicity slope introduces an additional uncertainty, the reported

trend can only be removed if the slope of the metallicity gradient are much steeper. However, the opposite seems to be the case for interacting galaxies (Kewley et al. 2010; Rupke, Kewley & Chien 2010; Rich et al. 2012). Therefore, we interpret the lower oxygen abundances as an indication of metal dilution through gas inflow by external gas accretion or tidal forces during strong galaxy interactions.

Letawe et al. (2007) also inferred oxygen abundances for their sample of luminous QSOs and found typically low abundances ( $12 + \log(\text{O}/\text{H}) < 8.6$ ) for their host galaxies. They attributed the lowest abundances to those host galaxies with distorted morphologies, and indeed observational and theoretical evidence is mounting that interactions can be responsible for the significant dilution of metals. For example, the central oxygen abundance is statistically lower by 0.05-0.1 dex in galaxies with close companions compared to isolated galaxies (Kewley et al. 2006; Ellison et al. 2008). Furthermore, Peebles, Pogge & Stanek (2009) and Sol Alonso, Michel-Dansac & Lambas (2010) found that the majority of extreme low-metallicity outliers from the mass-metallicity relation are distorted galaxies indicative of recent or ongoing interactions. The infall of gas is also an interpretation to explain the fundamental relation between mass, metallicity and SFR in galaxies (e.g. Manucci et al. 2010), in which galaxies with higher SFR at a given stellar mass have lower oxygen abundance. Montuori et al. (2010) showed with numerical simulations of galaxy mergers that a dilution in the central metallicity is expected to occur at various stages of galaxy interactions, even during fly-bys. However, the efficiency with which triggered star formation enriches the gas with metals again needs to be taken into account (Torrey et al. 2012). Finally, Yates, Kauffmann & Guo (2012) combined observations and semi-analytic models to show that massive galaxies with lower oxygen abundance had experienced a major merger in the past exhaust-



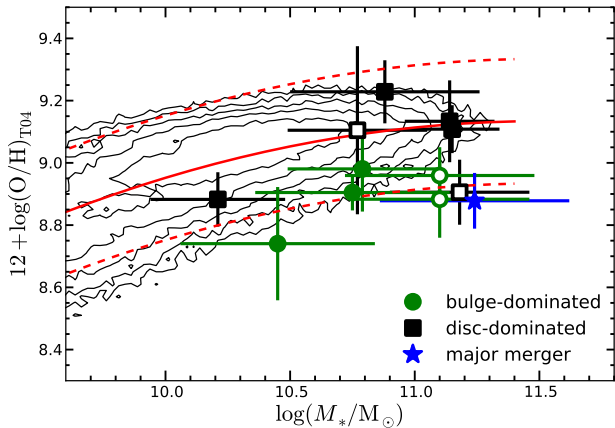


**Figure 10.** Oxygen abundance against the total stellar mass of QSO host galaxies. The oxygen abundances are extrapolated from  $1R_e$  towards the galaxy centre adopting the radius-metallicity slope of disc-dominated inactive galaxies presented by Sánchez et al. (2012b). Open and filled symbols correspond to oxygen abundance measurements based on the strong line NLR calibration of Storch-Bergmann et al. (1998) and the O3N2 calibration of Pettini & Pagel (2004), respectively. The symbols denote different galaxy morphologies as defined in Fig. 8. The distribution in oxygen abundances of star forming galaxies in the SDSS MPA/JHU galaxy catalogue (Tremonti et al. 2004) is shown as contours in a logarithmic scaling for comparison. The red solid line represents the best-fitting line to the SDSS data with the dashed lines indicating roughly its  $3\sigma$  uncertainty.

ing all the gas, but that subsequent accretion of low-metallicity gas leads to the gradual decline in abundances at the present time.

The systematically lower oxygen abundance of our bulge-dominated QSO host galaxies with respect to disc-dominated counterparts (at a given stellar mass) might be a common feature that coincides with ongoing star formation as the likely cause for their exceptionally blue colours (Jahnke, Kuhlbrodt & Wisotzki 2004). The gas inflow of low-metallicity gas on galaxy wide scales towards the centre of bulge-dominated systems might also be responsible for triggering the current phase of black hole accretion. Whether our bulge-dominated systems are currently in a late stage of a major merger after final coalescence, during a minor merger, or in a phase of gas accretion from the environment is something we cannot address with the current data. Contrary, the matching oxygen abundances and radial gradients for several disc-dominated QSO hosts with their inactive counterparts on galaxy wide scales suggest that their evolution is driven by internal galaxy processes that may also lead to the accretion on to the black hole.

## 6 SUMMARY AND CONCLUSIONS

In this paper we presented a comprehensive spatially resolved spectroscopic analysis of a flux-limited sample of QSOs at low redshift ( $z < 0.2$ ). It is the first paper of a series investigating in detail the properties of these QSO host galaxies. Here, we focused on the characterization of the spatially resolved ionized gas properties across the galaxies. The main results can be summarized as follows:

1. All QSO host galaxies exhibit ionized gas with a variety of ionization mechanisms from classical HII regions to ENLRs extending across the entire host galaxy.
2. The ENLR size, expressed as the [OIII] luminosity-weighted

ENLR radius ( $r_e$ ), strongly correlates with the intrinsic AGN luminosity as traced either by the continuum luminosity at  $5100\text{\AA}$  or by the integrated [OIII] luminosity. The scatter in the relation based on the [OIII] luminosity is significantly larger compared to the continuum luminosity, which indicates that the [OIII] luminosity does not solely depend on the AGN luminosity. We inferred a best-fitting relation of  $r_e \propto L_{5100}^{0.46 \pm 0.04}$ .

3. In more than 50 per cent of the host galaxies, irrespective of their morphology, we find ionized gas from HII-like regions indicating ongoing star formation. The specific star formation rates (SSFRs) based on the dust-corrected  $H\alpha$  luminosity are consistent with those of the star forming main sequence for most of these QSO hosts. Comparison with the SSFRs based on the  $60\mu\text{m}+100\mu\text{m}$  FIR luminosity suggests that the FIR luminosity is contaminated by AGN emission and  $H\alpha$  is a more robust and sensitive tracer for the current SFR. Significantly enhanced star formation is thus rare and always associated with strong galaxy interactions. The upper limits on the SSFR for the rest of our sample, including disc-dominated galaxies, place them clearly below the main sequence. Either their overall gas content is systematically lower or the star formation is possibly suppressed as a consequence of AGN feedback.

4. For a subsample of six QSO hosts we construct radial oxygen abundance gradients for the first time. The major merger exhibit a strong positive metallicity gradient in contrast to the negative gradients expected for undisturbed inactive disc-dominated QSO hosts. While the negative gradients in three disc-dominated hosts are statistically consistent with the reference slope despite a global metallicity offset, the slopes for the two bulge-dominated host galaxies are inconclusive.

5. Bulge-dominated QSO host galaxies exhibit systematically lower gas-phase oxygen abundances compared to their disc-dominated counterparts, placing them below the general mass-metallicity relation of galaxies. We interpret this as evidence for recent minor or advanced major mergers stages, which are causing the current metal dilution in these system.

The properties of the ionized gas draw a quite diverse picture of the population of nearby QSO host galaxies. Ionization from HII-like regions and AGN photoionization are found in host galaxies of different morphological types from disc- or bulge-dominated galaxies to strongly interacting systems. Several recent studies have suggested that there is no significant difference in the frequency of major-mergers between AGN and inactive galaxies (e.g. Cisternas et al. 2011; Kocevski et al. 2012; Böhm et al. 2013). On the contrary, a correlation between AGN fraction and various signatures of interaction, like close companions, ongoing mergers or post-merger systems has been reported (Koss et al. 2010; Ramos Almeida et al. 2010; Ellison et al. 2011; Bessiere et al. 2012; Cotini et al. 2013; Sabater, Best & Argudo-Fernández 2013). Deep AO-assisted NIR imaging of the luminous Palomar Green QSOs presented by Guyon, Sanders & Stockton (2006) shows that 30% of the galaxies are interacting systems and major mergers. One explanation for this apparent discrepancy is that selection effects of the samples play a crucial role and interaction and major-mergers only play a dominant role for the triggering the most luminous AGN (Treister et al. 2012). Our measurements of the gas-phase oxygen abundances in QSO hosts show that disc-dominated ones have matching properties to their inactive counterparts. This indicates that the QSO activity in disc-dominated AGN host galaxies is driven by internal galaxy processes. Interactions seem to play a crucial role not only for major-mergers, but also for the bulge-

dominated QSO hosts that may not have been fully accounted for in some imaging studies.

To understand whether and how quenching of star formation is related to AGN feedback, it will be crucial in the future to compare AGN with control samples of inactive galaxies that robustly match in most host galaxies properties. Our sample is too small in this respect given the diversity in the QSO host galaxies properties. However, the SSFRs in many of our disc-dominated QSO hosts match with those of inactive ones, while enhanced SSFRs are associated with mergers. It suggests that AGN only have little effect on the global SFR in these systems, at least during the current QSO phase. This appears in contrast with several studies that find strong evidence of AGN feedback. AGN-driven outflows have been identified in ULIRGs (e.g. Veilleux et al. 2013; Cicone et al. 2014) that can reach outflow velocities of  $1000 \text{ km s}^{-1}$  (e.g. Rupke & Veilleux 2011). Another indication for fast outflows are broad absorption line (BAL) QSOs which display very broad absorption lines with line widths of several thousand  $\text{km s}^{-1}$  (e.g. de Kool et al. 2001; Chartas et al. 2007).

Since our sample is selected solely based on optical QSO brightness at low redshifts, it does not contain any ULIRGs. Those are ongoing major mergers with a very high surface gas density leading to high SFR densities. The spatial scales of those outflows are often unconstrained and may not reach beyond 1 kpc in many cases. Despite the fact that our sample of QSOs is quite complementary to ULIRGs and BAL QSOs we are not able to resolve the central kpc around the QSOs. We are therefore blind to either circumnuclear starbursts or AGN-driven outflows on kpc scales that could still be present in our systems. On the other hand, we are able to characterise the properties of the entire host galaxies with 1-3 kpc resolution. If AGN-driven outflows would be present in all host galaxies system, its effect need to be restricted to the central kpc considering that the majority of galaxies show ionized gas and ongoing star formation across the entire host galaxies.

Identifying signatures of interactions solely based on broadband imaging data is often difficult given the low surface brightness of these features. Our results show that the properties of the gas-phase oxygen abundances may provide additional constraints on the occurrence of ongoing or past galaxy interactions, even for galaxies hosting a luminous QSO. Given that the emission lines usually have a higher surface brightness than the stellar continuum, it offers a high diagnostic value in particular with increasing redshifts. This will be important to construct robust AGN and inactive control samples separating the effects of internal galaxy processes and galaxy interactions when investigating the relation between AGN and their host galaxies. In particular for bulge-dominated galaxies, the oxygen abundance could provide additional diagnostic power to identify ongoing or recent interactions compared to pure imaging studies.

## ACKNOWLEDGEMENTS

We thank the referee for valuable comments and specific instructions that substantially improved the clarity of the paper. BH and LW acknowledge financial support by the DFG Priority Program 1177 “Witnesses of Cosmic History: Formation and evolution of black holes, galaxies and their environment”, grant Wi 1369/22-1 and Wi 1369/22-2. Furthermore, BH, DK and LW gratefully acknowledge the support by the DFG via grant Wi 1369/29-1. SFS would like to thanks the ‘Ministerio de Ciencia e Innovación’ project ICTS-2009-10, and the ‘Junta de Andalucía’ projects P08-

FWM-04319 and FQM360. DN and KJ are funded through the DFG Emmy Noether-Program, grant JA 1114/3-1. We like to thank J. Caruana and S. Dhawanfor checking the manuscript prior to submission.

## REFERENCES

- Alloin D., Collin-Souffrin S., Joly M., Vigroux L., 1979, A&A, 78, 200
- Annibali F., Bressan A., Rampazzo R., Zeilinger W. W., Vega O., Panuzzo P., 2010, A&A, 519, A40+
- Antonucci R., 1993, ARA&A, 31, 473
- Arribas S., Colina L., Monreal-Ibero A., Alfonso J., García-Marín M., Alonso-Herrero A., 2008, A&A, 479, 687
- Athey A. E., Bregman J. N., 2009, ApJ, 696, 681
- Baldwin J. A., Phillips M. M., Terlevich R., 1981, PASP, 93, 5
- Bell E. F., 2003, ApJ, 586, 794
- Bennert N., Canalizo G., Jungwiert B., Stockton A., Schweizer F., Peng C. Y., Lacy M., 2008, ApJ, 677, 846
- Bennert N., Falcke H., Schulz H., Wilson A. S., Wills B. J., 2002, ApJL, 574, L105
- Bentz M. C., Peterson B. M., Netzer H., Pogge R. W., Vestergaard M., 2009, ApJ, 697, 160
- Bertram T., Eckart A., Fischer S., Zuther J., Straubmeier C., Wisotzki L., Krips M., 2007, A&A, 470, 571
- Bessiere P. S., Tadhunter C. N., Ramos Almeida C., Villar Martín M., 2012, MNRAS, 426, 276
- Böhm A. et al., 2013, A&A, 549, A46
- Brinchmann J., Charlot S., White S. D. M., Tremonti C., Kauffmann G., Heckman T., Brinkmann J., 2004, MNRAS, 351, 1151
- Bruzual G., Charlot S., 2003, MNRAS, 344, 1000
- Buckley J., James I., 1979, Biometrika, 66, 429
- Calzetti D., Armus L., Bohlin R. C., Kinney A. L., Koornneef J., Storchi-Bergmann T., 2000, ApJ, 533, 682
- Canalizo G., Stockton A., 2001, ApJ, 555, 719
- Canalizo G., Stockton A., 2013, ArXiv e-prints
- Caon N., Macchetto D., Pastoriza M., 2000, ApJS, 127, 39
- Cappellari M., Copin Y., 2003, MNRAS, 342, 345
- Cardelli J. A., Clayton G. C., Mathis J. S., 1989, ApJ, 345, 245
- Chartas G., Brandt W. N., Gallagher S. C., Proga D., 2007, AJ, 133, 1849
- Christensen L., Jahnke K., Wisotzki L., Sánchez S. F., 2006, A&A, 459, 717
- Cicone C. et al., 2014, A&A, 562, A21
- Cid Fernandes R., Gu Q., Melnick J., Terlevich E., Terlevich R., Kunth D., Rodrigues Lacerda R., Joguet B., 2004, MNRAS, 355, 273
- Cid Fernandes R., Mateus A., Sodré L., Stasińska G., Gomes J. M., 2005, MNRAS, 358, 363
- Cid Fernandes R. et al., 2013, ArXiv e-prints
- Cid Fernandes R., Stasińska G., Schlickmann M. S., Mateus A., Vale Asari N., Schoenell W., Sodré L., 2010, MNRAS, 403, 1036
- Cisternas M. et al., 2011, ApJ, 726, 57
- Clark N. E., Axon D. J., Tadhunter C. N., Robinson A., O’Brien P., 1998, ApJ, 494, 546
- Condon J. J., Cotton W. D., Greisen E. W., Yin Q. F., Perley R. A., Taylor G. B., Broderick J. J., 1998, AJ, 115, 1693
- Cotini S., Ripamonti E., Caccianiga A., Colpi M., Della Ceca R., Mapelli M., Severgnini P., Segreto A., 2013, MNRAS, 431, 2661
- Davis T. A. et al., 2011, MNRAS, 417, 882

- de Kool M., Arav N., Becker R. H., Gregg M. D., White R. L., Laurent-Muehleisen S. A., Price T., Korista K. T., 2001, *ApJ*, 548, 609
- Denicoló G., Terlevich R., Terlevich E., 2002, *MNRAS*, 330, 69
- Diehl S., Statler T. S., 2006, *MNRAS*, 368, 497
- Domínguez Sánchez H. et al., 2012, *MNRAS*, 426, 330
- Dopita M. A., Evans I. N., 1986, *ApJ*, 307, 431
- Dumas G., Mundell C. G., Emsellem E., Nagar N. M., 2007, *MNRAS*, 379, 1249
- Dunlop J. S., McLure R. J., Kukula M. J., Baum S. A., O’Dea C. P., Hughes D. H., 2003, *MNRAS*, 340, 1095
- Edmunds M. G., Pagel B. E. J., 1984, *MNRAS*, 211, 507
- Ellison S. L., Patton D. R., Mendel J. T., Scudder J. M., 2011, *MNRAS*, 418, 2043
- Ellison S. L., Patton D. R., Simard L., McConnachie A. W., 2008, *AJ*, 135, 1877
- Emsellem E. et al., 2004, *MNRAS*, 352, 721
- Fraquelli H. A., Storchi-Bergmann T., Levenson N. A., 2003, *MNRAS*, 341, 449
- Fruchter A. S., Hook R. N., 2002, *PASP*, 114, 144
- Gabor J. M. et al., 2009, *ApJ*, 691, 705
- Gerssen J., Allington-Smith J., Miller B. W., Turner J. E. H., Walker A., 2006, *MNRAS*, 365, 29
- González Delgado R. M., Cerviño M., Martins L. P., Leitherer C., Hauschildt P. H., 2005, *MNRAS*, 357, 945
- Goudfrooij P., Hansen L., Jorgensen H. E., Norgaard-Nielsen H. U., 1994, *A&AS*, 105, 341
- Greene J. E., Zakamska N. L., Ho L. C., Barth A. J., 2011, *ApJ*, 732, 9
- Grogin N. A. et al., 2005, *ApJL*, 627, L97
- Guyon O., Sanders D. B., Stockton A., 2006, *ApJS*, 166, 89
- Hainline K. N., Hickox R., Greene J. E., Myers A. D., Zakamska N. L., 2013, *ApJ*, 774, 145
- Heckman T. M., 1980, *A&A*, 87, 152
- Helou G., Khan I. R., Malek L., Boehmer L., 1988, *ApJS*, 68, 151
- Henry R. B. C., Worthey G., 1999, *PASP*, 111, 919
- Ho L. C., 2005, *ApJ*, 629, 680
- Hopkins P. F., Somerville R. S., Hernquist L., Cox T. J., Robertson B., Li Y., 2006, *ApJ*, 652, 864
- Horne K., 1986, *PASP*, 98, 609
- Humphrey A., Villar-Martín M., Sánchez S. F., Martínez-Sansigre A., Delgado R. G., Pérez E., Tadhunter C., Pérez-Torres M. A., 2010, *MNRAS*, 408, L1
- Husemann B. et al., 2013a, *A&A*, 549, A87
- Husemann B., Kamann S., Sandin C., Sánchez S. F., García-Benito R., Mast D., 2012, *A&A*, 545, A137
- Husemann B., Sánchez S. F., Wisotzki L., Jahnke K., Kupko D., Nugroho D., Schramm M., 2010, *A&A*, 519, A115+
- Husemann B., Wisotzki L., Jahnke K., Sánchez S. F., 2011, *A&A*, 535, A72
- Husemann B., Wisotzki L., Sánchez S. F., Jahnke K., 2008, *A&A*, 488, 145
- Husemann B., Wisotzki L., Sánchez S. F., Jahnke K., 2013b, *A&A*, 549, A43
- Hutchings J. B., Neff S. G., 1992, *AJ*, 104, 1
- Isobe T., Feigelson E. D., Nelson P. I., 1986, *ApJ*, 306, 490
- Jahnke K., Kuhlbrodt B., Wisotzki L., 2004, *MNRAS*, 352, 399
- Jahnke K. et al., 2004a, *ApJ*, 614, 568
- Jahnke K., Wisotzki L., Courbin F., Letawe G., 2007, *MNRAS*, 378, 23
- Jahnke K., Wisotzki L., Sánchez S. F., Christensen L., Becker T., Kelz A., Roth M. M., 2004b, *AN*, 325, 128
- Kauffmann G. et al., 2003, *MNRAS*, 346, 1055
- Kellermann K. I., Sramek R., Schmidt M., Shaffer D. B., Green R., 1989, *AJ*, 98, 1195
- Kennicutt, Jr. R. C., 1998, *ApJ*, 498, 541
- Kennicutt, Jr. R. C., Bresolin F., Garnett D. R., 2003, *ApJ*, 591, 801
- Kennicutt, Jr. R. C., Garnett D. R., 1996, *ApJ*, 456, 504
- Kewley L. J., Dopita M. A., 2002, *ApJS*, 142, 35
- Kewley L. J., Dopita M. A., Sutherland R. S., Heisler C. A., Trevena J., 2001, *ApJ*, 556, 121
- Kewley L. J., Ellison S. L., 2008, *ApJ*, 681, 1183
- Kewley L. J., Geller M. J., Jansen R. A., Dopita M. A., 2002, *AJ*, 124, 3135
- Kewley L. J., Groves B., Kauffmann G., Heckman T., 2006, *MNRAS*, 372, 961
- Kewley L. J., Rupke D., Jabran Zahid H., Geller M. J., Barton E. J., 2010, *ApJL*, 721, L48
- Kim M., Ho L. C., Im M., 2006, *ApJ*, 642, 702
- Kocevski D. D. et al., 2012, *ApJ*, 744, 148
- Köhler T., Groote D., Reimers D., Wisotzki L., 1997, *A&A*, 325, 502
- Koss M., Mushotzky R., Veilleux S., Winter L., 2010, *ApJL*, 716, L125
- Krist J., 1995, in *Astronomical Society of the Pacific Conference Series*, Vol. 77, *Astronomical Data Analysis Software and Systems IV*, Shaw R. A., Payne H. E., Hayes J. J. E., eds., pp. 349–
- Lacy M., Sajina A., Petric A. O., Seymour N., Canalizo G., Ridgway S. E., Armus L., Storrie-Lombardi L. J., 2007, *ApJL*, 669, L61
- Lavalley M., Isobe T., Feigelson E., 1992, in *Astronomical Society of the Pacific Conference Series*, Vol. 25, *Astronomical Data Analysis Software and Systems I*, D. M. Worrall, C. Biemesderfer, & J. Barnes, ed., pp. 245–
- Le Fèvre O. et al., 2003, in *Society of Photo-Optical Instrumentation Engineers (SPIE) Conference Series*, Vol. 4841, *Society of Photo-Optical Instrumentation Engineers (SPIE) Conference Series*, M. Iye & A. F. M. Moorwood, ed., pp. 1670–1681
- Letawe G., Magain P., Courbin F., Jablonka P., Jahnke K., Meylan G., Wisotzki L., 2007, *MNRAS*, 378, 83
- Li C., Kauffmann G., Heckman T. M., White S. D. M., Jing Y. P., 2008, *MNRAS*, 385, 1915
- Liang Y. C., Yin S. Y., Hammer F., Deng L. C., Flores H., Zhang B., 2006, *ApJ*, 652, 257
- Liu G., Zakamska N. L., Greene J. E., Nesvadba N. P. H., Liu X., 2013, *MNRAS*, 430, 2327
- López-Sánchez Á. R., Dopita M. A., Kewley L. J., Zahid H. J., Nicholls D. C., Scharwächter J., 2012, *MNRAS*, 426, 2630
- Macchetto F., Pastoriza M., Caon N., Sparks W. B., Giallisco M., Bender R., Capaccioli M., 1996, *A&AS*, 120, 463
- Magrini L., Vilchez J. M., Mampaso A., Corradi R. L. M., Leisy P., 2007, *A&A*, 470, 865
- Mannucci F., Cresci G., Maiolino R., Marconi A., Gnerucci A., 2010, *MNRAS*, 408, 2115
- Martins L. P., González Delgado R. M., Leitherer C., Cerviño M., Hauschildt P., 2005, *MNRAS*, 358, 49
- Mast D. et al., 2014, *A&A*, 561, A129
- McCall M. L., Rybski P. M., Shields G. A., 1985, *ApJS*, 57, 1
- McCarthy P. J., van Breugel W., Spinrad H., Djorgovski S., 1987, *ApJL*, 321, L29
- McDermid R. M. et al., 2006, *MNRAS*, 373, 906
- Montuori M., Di Matteo P., Lehnert M. D., Combes F., Semelin B., 2010, *A&A*, 518, A56+

- Morganti R., Tadhunter C. N., Dickson R., Shaw M., 1997, *A&A*, 326, 130
- Moshir M., et al., 1990, in *IRAS Faint Source Catalogue*, version 2.0 (1990), p. 0
- Moy E., Rocca-Volmerange B., 2002, *A&A*, 383, 46
- Mullaney J. R., Alexander D. M., Fine S., Goulding A. D., Harrison C. M., Hickox R. C., 2013, *MNRAS*, 433, 622
- Netzer H. et al., 2007, *ApJ*, 666, 806
- Osterbrock D. E., Ferland G. J., 2006, *Astrophysics of gaseous nebulae and active galactic nuclei*. 2nd. ed. by D.E. Osterbrock and G.J. Ferland. Sausalito, CA: University Science Books, 2006
- Pagel B. E. J., Edmunds M. G., Blackwell D. E., Chun M. S., Smith G., 1979, *MNRAS*, 189, 95
- Pagel B. E. J., Edmunds M. G., Smith G., 1980, *MNRAS*, 193, 219
- Peebles M. S., Pogge R. W., Stanek K. Z., 2009, *ApJ*, 695, 259
- Peng C. Y., Ho L. C., Impey C. D., Rix H., 2010, *AJ*, 139, 2097
- Peng C. Y., Ho L. C., Impey C. D., Rix H.-W., 2002, *AJ*, 124, 266
- Pérez-Montero E., Díaz A. I., 2005, *MNRAS*, 361, 1063
- Pettini M., Pagel B. E. J., 2004, *MNRAS*, 348, L59
- Pilyugin L. S., 2001, *A&A*, 369, 594
- Pilyugin L. S., Thuan T. X., 2005, *ApJ*, 631, 231
- Ramos Almeida C., Tadhunter C. N., Inskip K. J., Morganti R., Holt J., Dicken D., 2010, *MNRAS*, 1609
- Reimers D., Koehler T., Wisotzki L., 1996, *A&AS*, 115, 235
- Rich J. A., Torrey P., Kewley L. J., Dopita M. A., Rupke D. S. N., 2012, *ApJ*, 753, 5
- Rosales-Ortega F. F., Sánchez S. F., Iglesias-Páramo J., Díaz A. I., Vílchez J. M., Bland-Hawthorn J., Husemann B., Mast D., 2012, *ApJL*, 756, L31
- Rosario D. J. et al., 2012, *A&A*, 545, A45
- Rosario D. J., Whittle M., Nelson C. H., Wilson A. S., 2010, *ApJL*, 711, L94
- Rupke D. S. N., Kewley L. J., Chien L., 2010, *ApJ*, 723, 1255
- Rupke D. S. N., Veilleux S., 2011, *ApJL*, 729, L27
- Sabater J., Best P. N., Argudo-Fernández M., 2013, *MNRAS*, 430, 638
- Sánchez S. F., Garcia-Lorenzo B., Mediavilla E., González-Serrano J. I., Christensen L., 2004a, *ApJ*, 615, 156
- Sánchez S. F. et al., 2004b, *ApJ*, 614, 586
- Sánchez S. F. et al., 2012a, *A&A*, 538, A8
- Sánchez S. F. et al., 2012b, *A&A*, 546, A2
- Sanders D. B., Soifer B. T., Elias J. H., Madore B. F., Matthews K., Neugebauer G., Scoville N. Z., 1988a, *ApJ*, 325, 74
- Sanders D. B., Soifer B. T., Elias J. H., Neugebauer G., Matthews K., 1988b, *ApJL*, 328, L35
- Santini P. et al., 2012, *A&A*, 540, A109
- Sarzi M. et al., 2006, *MNRAS*, 366, 1151
- Schawinski K., Simmons B. D., Urry C. M., Treister E., Glikman E., 2012, *MNRAS*, 425, L61
- Schlegel D. J., Finkbeiner D. P., Davis M., 1998, *ApJ*, 500, 525
- Schmitt H. R., Donley J. L., Antonucci R. R. J., Hutchings J. B., Kinney A. L., Pringle J. E., 2003, *ApJ*, 597, 768
- Schramm M., Wisotzki L., Jahnke K., 2008, *A&A*, 478, 311
- Schweitzer M. et al., 2006, *ApJ*, 649, 79
- Silverman J. D. et al., 2009, *ApJ*, 696, 396
- Sol Alonso M., Michel-Dansac L., Lambas D. G., 2010, *A&A*, 514, A57+
- Stern J., Laor A., 2013, *MNRAS*, 431, 836
- Stockton A., MacKenty J. W., 1987, *ApJ*, 316, 584
- Stoklasová I., Ferruit P., Emsellem E., Jungwiert B., Pécontal E., Sánchez S. F., 2009, *A&A*, 500, 1287
- Storchi-Bergmann T., Calzetti D., Kinney A. L., 1994, *ApJ*, 429, 572
- Storchi-Bergmann T., Schmitt H. R., Calzetti D., Kinney A. L., 1998, *AJ*, 115, 909
- Tal T., van Dokkum P. G., Nelan J., Bezanson R., 2009, *AJ*, 138, 1417
- Torrey P., Cox T. J., Kewley L., Hernquist L., 2012, *ApJ*, 746, 108
- Trager S. C., Faber S. M., Worthey G., González J. J., 2000, *AJ*, 119, 1645
- Treister E., Schawinski K., Urry C. M., Simmons B. D., 2012, *ApJL*, 758, L39
- Tremonti C. A. et al., 2004, *ApJ*, 613, 898
- Trinchieri G., di Serego Alighieri S., 1991, *AJ*, 101, 1647
- Unger S. W., Pedlar A., Axon D. J., Whittle M., Meurs E. J. A., Ward M. J., 1987, *MNRAS*, 228, 671
- Urrutia T., Lacy M., Spoon H., Glikman E., Petric A., Schulz B., 2012, *ApJ*, 757, 125
- Valdes F., Gupta R., Rose J. A., Singh H. P., Bell D. J., 2004, *ApJS*, 152, 251
- Veilleux S. et al., 2009, *ApJ*, 701, 587
- Veilleux S. et al., 2013, *ApJ*, 776, 27
- Viironen K., Delgado-Inglada G., Mampaso A., Magrini L., Corradi R. L. M., 2007, *MNRAS*, 381, 1719
- Vila-Costas M. B., Edmunds M. G., 1992, *MNRAS*, 259, 121
- Villar-Martín M., Tadhunter C., Humphrey A., Encina R. F., Delgado R. G., Torres M. P., Martínez-Sansigre A., 2011, *MNRAS*, 416, 262
- Villar-Martín M., Tadhunter C., Morganti R., Axon D., Koeke-moer A., 1999, *MNRAS*, 307, 24
- Villar-Martín M., Tadhunter C., Pérez E., Humphrey A., Martínez-Sansigre A., Delgado R. G., Pérez-Torres M., 2010, *MNRAS*, 407, L6
- Villforth C. et al., 2014, *MNRAS*, 439, 3342
- Wild V., Heckman T., Charlot S., 2010, *MNRAS*, 405, 933
- Winter L. M., Lewis K. T., Koss M., Veilleux S., Keeney B., Mushotzky R. F., 2010, *ApJ*, 710, 503
- Wisotzki L., Christlieb N., Bade N., Beckmann V., Köhler T., Vanelle C., Reimers D., 2000, *A&A*, 358, 77
- Wisotzki L., Koehler T., Groote D., Reimers D., 1996, *A&AS*, 115, 227
- Wold I., Sheinis A. I., Wolf M. J., Hooper E. J., 2010, *MNRAS*, 1374
- Worthey G., 1994, *ApJS*, 95, 107
- Wu Q., 2009, *MNRAS*, 398, 1905
- Yates R. M., Kauffmann G., Guo Q., 2012, *MNRAS*, 422, 215
- Yuan T.-T., Kewley L. J., Rich J., 2013, *ApJ*, 767, 106
- Zakamska N. L. et al., 2006, *AJ*, 132, 1496
- Zaritsky D., Kennicutt, Jr. R. C., Huchra J. P., 1994, *ApJ*, 420, 87

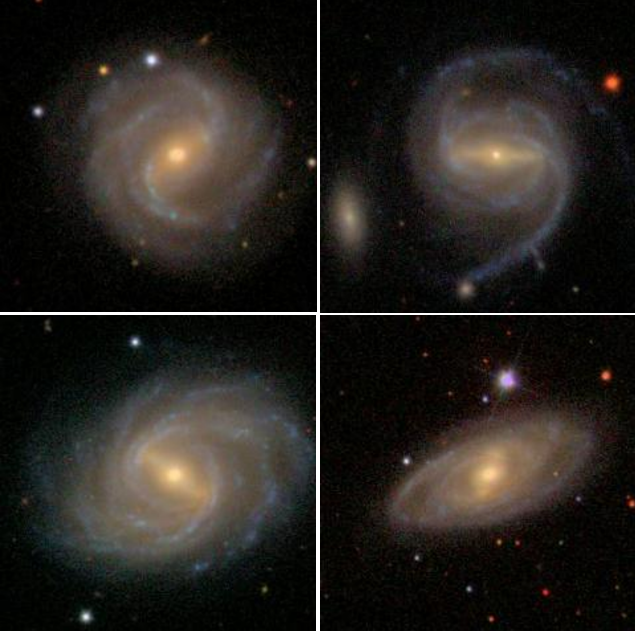


**Figure A1.** SDSS colour images of CALIFA galaxies used for simulating QSO host galaxies at various redshift. The chosen galaxies are NGC 0776 (upper left), NGC 5000 (upper right), NGC 5406 (lower left), and NGC 6497 (lower right).

## APPENDIX A: ESTIMATING SYSTEMATIC UNCERTAINTIES OF THE QSO-HOST DEBLENDING PROCESS

### A1 Simulation of realistic IFU data

Simulating realistic IFU data to estimate the systematic uncertainties of the QSO-host deblending process is a difficult task. Details of the 2D host galaxy surface brightness distribution, the 2D gas kinematics, the ionized gas distribution and brightness, the apparent host galaxy brightness, the nucleus-to-host ratio, the shape of QSO spectrum and the spatial resolution are all affecting the result of the deblending process to some extent. Since this study is the first one to characterize QSO host galaxies in such details, it is impossible to create mock data based on an analytic prescription of those components.

Here, we took advantage of the CALIFA survey (Sánchez et al. 2012a) that already provided IFU data for 100 galaxies with its first data release (Husmann et al. 2013a). We selected 4 different nearby face-on spiral galaxies (see Fig. A1) with stellar masses between  $2 \times 10^{10} M_{\odot}$  and  $10^{11} M_{\odot}$  which all display significant star formation as seen through the strong  $H\alpha$  emission. Those galaxies serve as our empirical models for the QSO host galaxies simulations. Our template CALIFA galaxies are rather local galaxies with  $z < 0.02$  which provide much higher spatial resolution as our VIMOS data at higher redshifts. We therefore binned the CALIFA data by 2-10 spaxels to simulate higher redshift galaxies. Each binning corresponds to a certain redshift considering the ratio of the  $1''$  CALIFA and  $0.67''$  VIMOS sampling and the ratio of the physical half light radius between the CALIFA galaxies and the targeted half light radius. We additionally smoothed the data by a 2D Gaussian so that the PSF of the simulated data match with the median seeing of our VIMOS observation ( $1.6''$  along right ascension and  $1.2''$  along declination). In order to scale the apparent host galaxy brightness independently from the ionized gas, we modelled the stellar con-

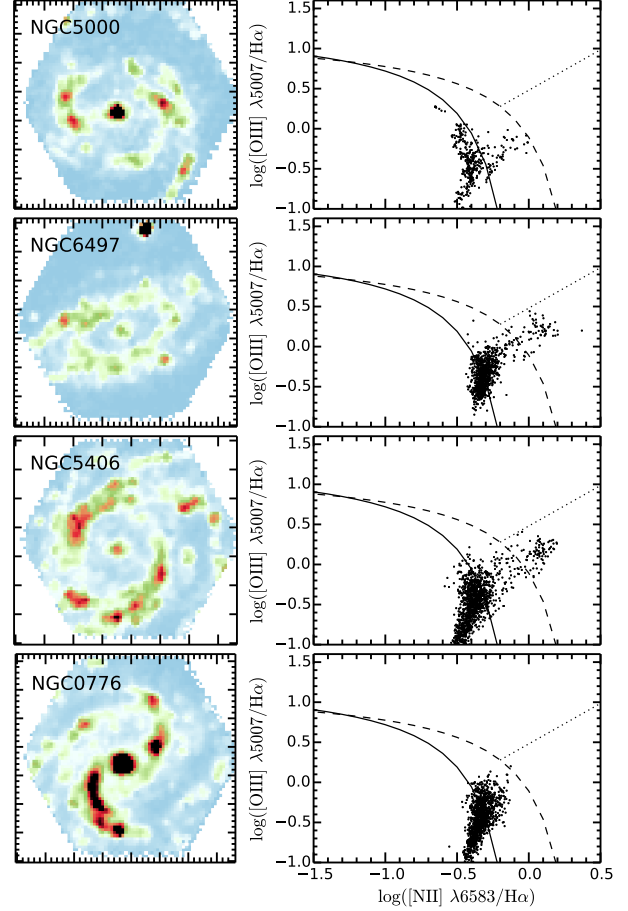


**Figure A2.** *Left panels:* Reconstructed  $H\alpha$  narrow-band images of the CALIFA galaxies after stellar continuum subtraction. *Right panels:* Standard BPT diagnostic diagram for all spaxels in the CALIFA cubes which have a  $S/N > 3$ .

tinuum and ionized gas in the CALIFA data. Finally, we placed a high S/N QSO spectrum data at the centre of the simulated galaxy taken a certain nucleus-to-host ratio into account and added noise to the simulated cube matching with the depth of the VIMOS data.

Based on this scheme we ran a suite of simulations to produce QSO host galaxies based on all four CALIFA galaxies with the following parameters. The apparent  $V$  band host galaxy brightness was set to 15.0, 16.0, 16.5, and 17.0 mag at any redshift. The  $H\alpha$  luminosity was set to 0.25, 1, 4 and 16 times the  $H\alpha$  luminosity of the corresponding CALIFA galaxy. We used four different QSOs, namely HE 1019–1441, HE 1029–1401, HE 1239–2624, and HE 1338–1423, to add a QSO component to the simulations with nucleus-to-host ratios of 0.25, 1, 2, and 4 at the corresponding host galaxy brightness. All galaxies are simulated by assuming a half light radius of 5 and 10 kpc to cover very roughly the physical sizes of the QSO host galaxies in our sample. Afterwards we ran the QSO-host deblending process on each simulated galaxy with QDBLEND<sup>3D</sup> and recovered the  $V$  band host galaxy brightness. We further binned the simulated data by  $3 \times 3$  spaxels to mimic our binning scheme before the stellar continuum and emission lines analysis. From that analysis we measured the total  $H\alpha$  luminosity and the oxygen abundance at the half light radius which are the main observables from which we draw our main conclusions.



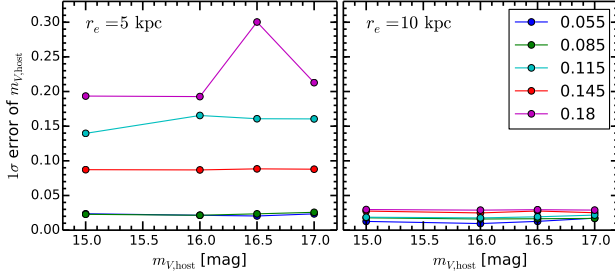


**Figure A3.** Recovered  $1\sigma$  uncertainty of the host galaxy brightness after the QSO-host deblending process. We present the results for galaxies with  $r_e = 5$  kpc (left panel) and  $r_e = 10$  kpc (right panel). The uncertainty of the recovered host galaxy brightness is plotted against the input host galaxy brightness for five different redshifts, 0.054, 0.085, 0.115, 0.145, 0.18, respectively. We find no significant dependence on the nucleus-to-host ratio and therefore do not show it in the plots.

## A2 Systematic uncertainties of the host galaxy brightness

Although the recovery of the host galaxy brightness is not a primary quantity for the presented work, we still want to assess the uncertainty introduced by the QSO-host deblending technique. A similar assessment of the uncertainties for the broad-band imaging decomposition (Jahnke, Kuhlbrodt & Wisotzki 2004) lead to an average error of 0.1 mag. Instead of computing the average uncertainty we provide the results for the full parameter space covered by our simulation. We show the results in Fig. A3 for the two different galaxy sizes with effective radii of  $r_e = 5$  kpc (left panel) and  $r_e = 10$  kpc (right panel). We ignore the nucleus-to-host ratio within the range of our simulation, since we find no significant trend of the uncertainty with the nucleus-to-host ratio.

The primary driver of the uncertainty in the host galaxy brightness is the redshift and the size of the galaxy. It is a natural consequence of the QSO-host deblending of seeing-limited observations, because the QSO contamination covers an apparently larger part of the galaxy when the host galaxy become small or it is apparent size decreases with redshift. For galaxies with  $r_e = 5$  kpc at about a redshift of 0.11, we estimate a  $V$ -band uncertainty of 0.1 mag in agreement with the results of the broad-band imaging studies. Those kind of galaxies represent the majority of our systems, but we also have larger galaxies at lower redshifts in the sample for which the systematic uncertainty in the galaxy brightness will be significantly lower.

In Fig. 2 we provide the convolved error bars of the measurement and systematic errors as derived from the simulation at the matched galaxy properties. Since Jahnke, Kuhlbrodt & Wisotzki (2004) reported only a fixed systematic uncertainty, we decided to use the uncertainties derived for the IFU data also for the broad-band imaging data to be conservative. We would expect that the systematic uncertainties in the IFU QSO-host deblending scheme are equal or worse than those of the broad-band imaging study.

## A3 Systematic uncertainties of the extinction-corrected SFR

The systematic uncertainties of the extinction-corrected SFR depend on the recovered  $H\alpha$  flux and the measurement accuracy of the  $H\beta/H\alpha$  Balmer decrement to apply the extinction-correction. Both measurements may react differently on the QSO-host deblending. We are not trying to disentangle both effects, but quantify the combined systematics effects on the measured extinction-corrected  $H\alpha$  luminosity.

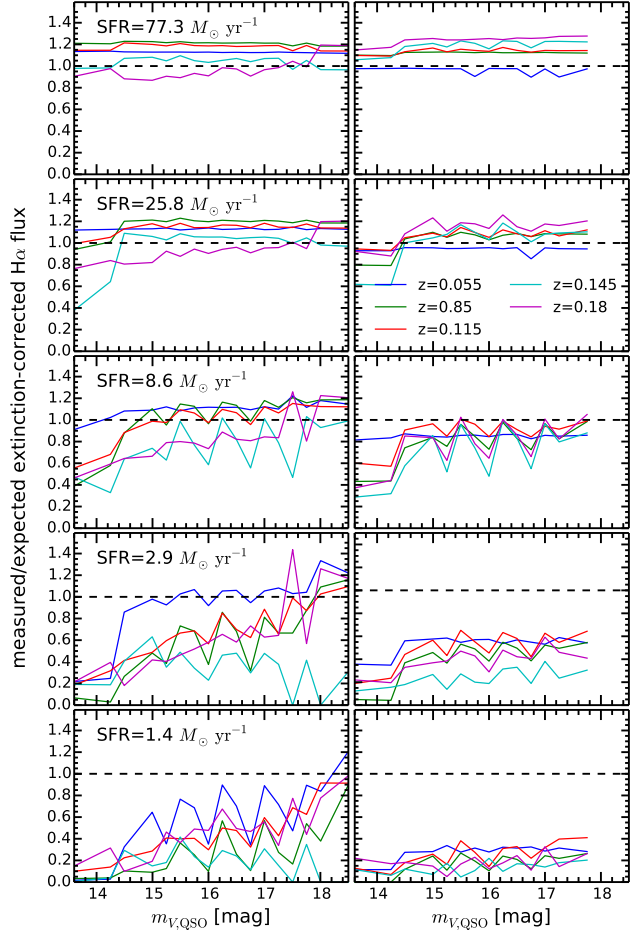


**Figure A4.** Result for the recovery of the extinction-corrected  $H\alpha$  luminosity from the simulation. The ratio between measured and expected extinction-corrected  $H\alpha$  luminosity is shown as a function of QSO brightness. Different coloured lines correspond to redshifts of 0.055, 0.085, 0.115, 0.145 and 0.185 as indicated in the legend. The left panels correspond to galaxies with an effective radius of  $r_e = 5$  kpc and the right panels to the ones with  $r_e = 10$  kpc. The dashed black lines indicate the best case of a 100% recovery of the  $H\alpha$  luminosity.

In Fig. A4 we show the ratio between the measured and expected extinction-corrected  $H\alpha$  luminosity as a function of  $V$ -band QSO brightness for galaxies placed at redshifts 0.055, 0.085, 0.115, 0.145 and 0.18. We present the results for the two intrinsic galaxy sizes  $r_e = 5$  kpc (left panels) and  $r_e = 10$  kpc (right panels) as well as for five different input SFRs of  $1.3 M_\odot \text{ yr}^{-1}$ ,  $2.7 M_\odot \text{ yr}^{-1}$ ,  $8.0 M_\odot \text{ yr}^{-1}$ ,  $23.9 M_\odot \text{ yr}^{-1}$ , and  $71.6 M_\odot \text{ yr}^{-1}$ .

We find that the  $H\alpha$  luminosity is severely underestimated for the lowest SFR at high redshifts as expected because part of the  $H\alpha$  flux fall below the S/N limit of the observations. There is also a trend with QSO brightness in the sense that  $H\alpha$  luminosity is better recovered for fainter QSOs, which disappears with increasing SFR. It is easy to understand that the contrast between the QSO emission and the  $H\alpha$  flux in the host galaxy determines how well the host galaxy emission can be recovered close to the QSO nucleus. In addition the size of the galaxy matters. The QSO will affect a smaller region of host galaxy with increasing size so that total  $H\alpha$  flux of the host galaxy can be better recovered.

Based on these simulation we take the systematics into ac-

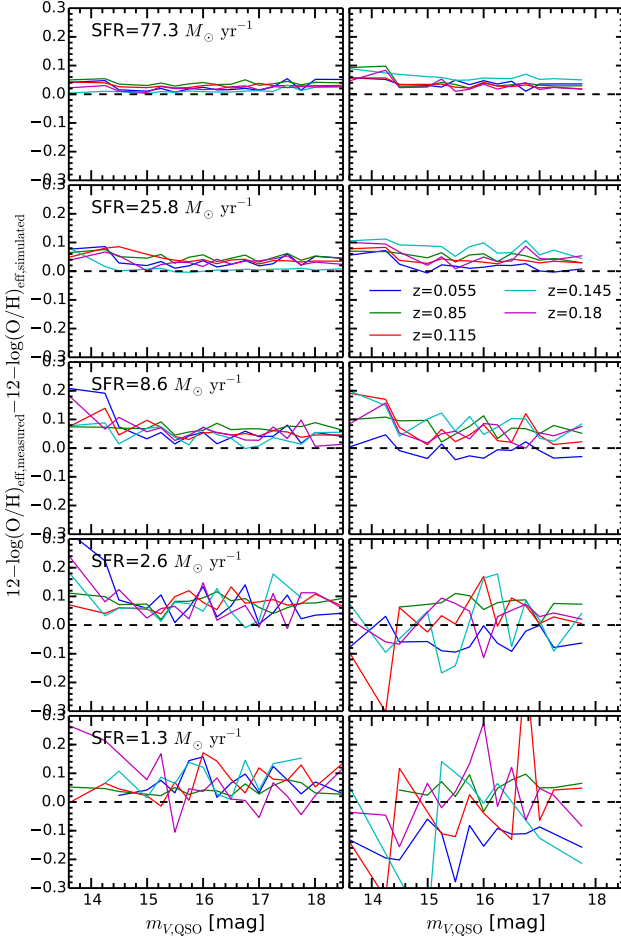


**Figure A5.** Result for the recovery of the oxygen abundance  $12 + \log(\text{O}/\text{H})$  from the simulation. The difference between measured and simulated oxygen abundance is shown as a function of QSO brightness. Different coloured lines correspond to redshifts of 0.055, 0.085, 0.115, 0.145 and 0.185 as indicated in the legend. The left panels correspond to galaxies with an effective radius of  $r_e = 5$  kpc and the right panels to the ones with  $r_e = 10$  kpc. The dashed black lines correspond to the case where the measured and simulated oxygen abundance matches one-to-one.

count for each object individually by correcting the measured SFR according to the QSO brightness, galaxy size, redshift and level of SFR. Furthermore, we include the systematic uncertainty of the correction into the error budget.

#### A4 Systematic uncertainties of the oxygen abundance

The systematic effects on the measured oxygen abundance are presented in Fig. A5. We estimate the oxygen abundance at the effective radius  $r_e$ . Depending on the galaxy size and redshift, it is less affected by the QSO-host deblending process unless the effective radius becomes smaller than the seeing disc. Those resolution effects were specifically studied by Yuan, Kewley & Rich (2013) and Mast et al. (2014) as function of redshift. They found that spatial resolution has a strong impact on the recovered metallicity gradients.

Our simulations show that the oxygen abundance at a fixed radius is more strongly affected with increasing redshift and at low S/N parametrized by the SFR. There is a trend to overestimate the

oxygen abundance with increasing redshift, which is caused by the luminosity weighting of the beam smearing towards the galaxy centre with higher intrinsic oxygen abundance. S/N effects obviously set in at very low SFRs at high redshifts. The effect of the QSO-host deblending seems to start playing a more significant role at a V-band QSO brightness of  $< 15$  mag.

For galaxies with  $z < 0.1$  the measured and simulated oxygen abundance agree within the errors for almost all host galaxy parameters covered, which represent the majority of our galaxies. The systematic error on the measurements vary between 0.03 and 0.15 with redshift and host galaxy properties and we include those systematic errors into the uncertainties determined individually for each object.

## APPENDIX B: RESULTS OF THE SPECTRAL QSO-HOST DEBLENDING

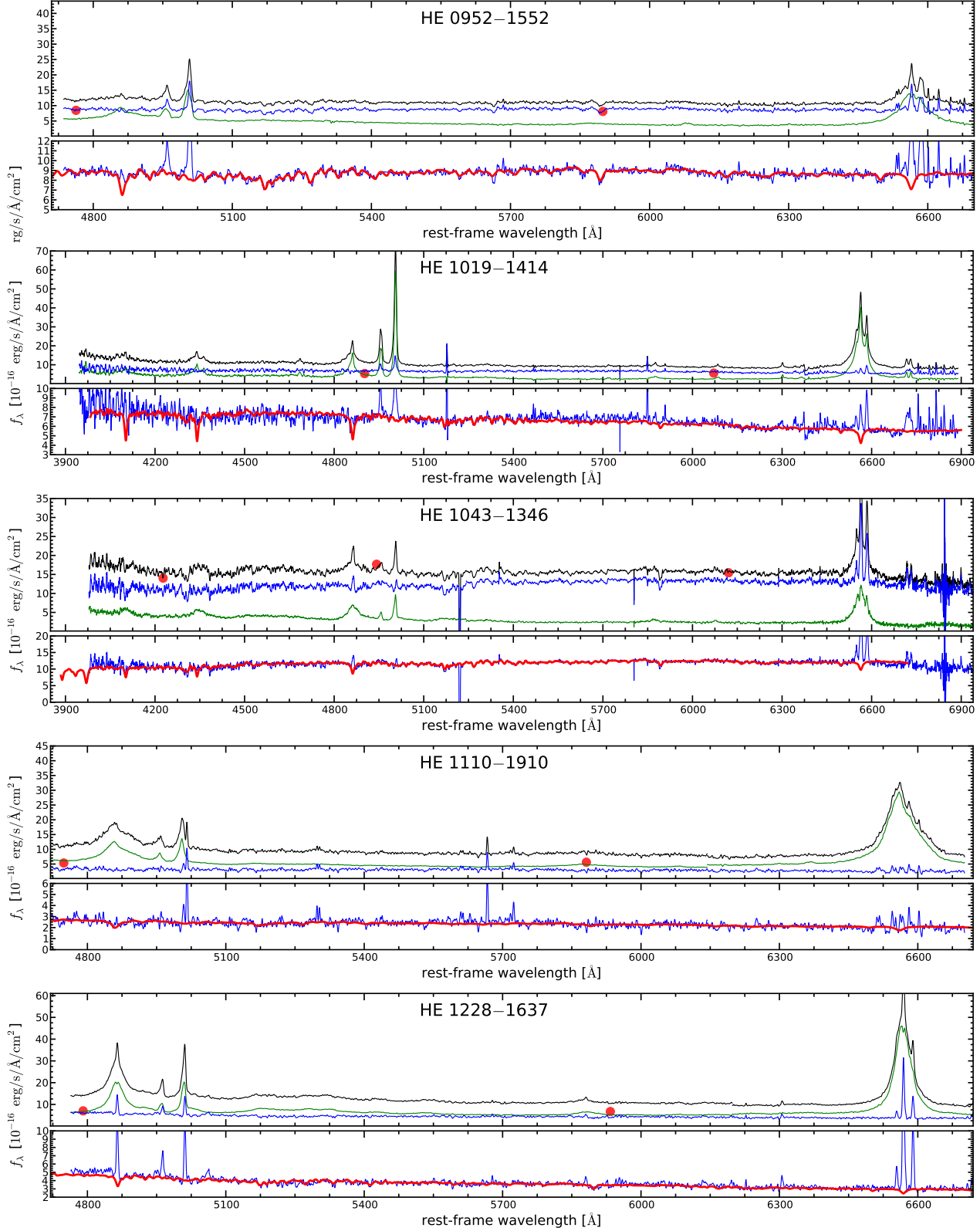


**Figure B1.** Results of the spectral QSO-host deblending. The black line corresponds to the integrated spectrum, the green line to the QSO contribution and the blue line to the host galaxy contribution. The bottom panels show the host galaxy continuum emission with the best-fitting model spectrum (see Section 4.1 for details) overlaid as the red line.



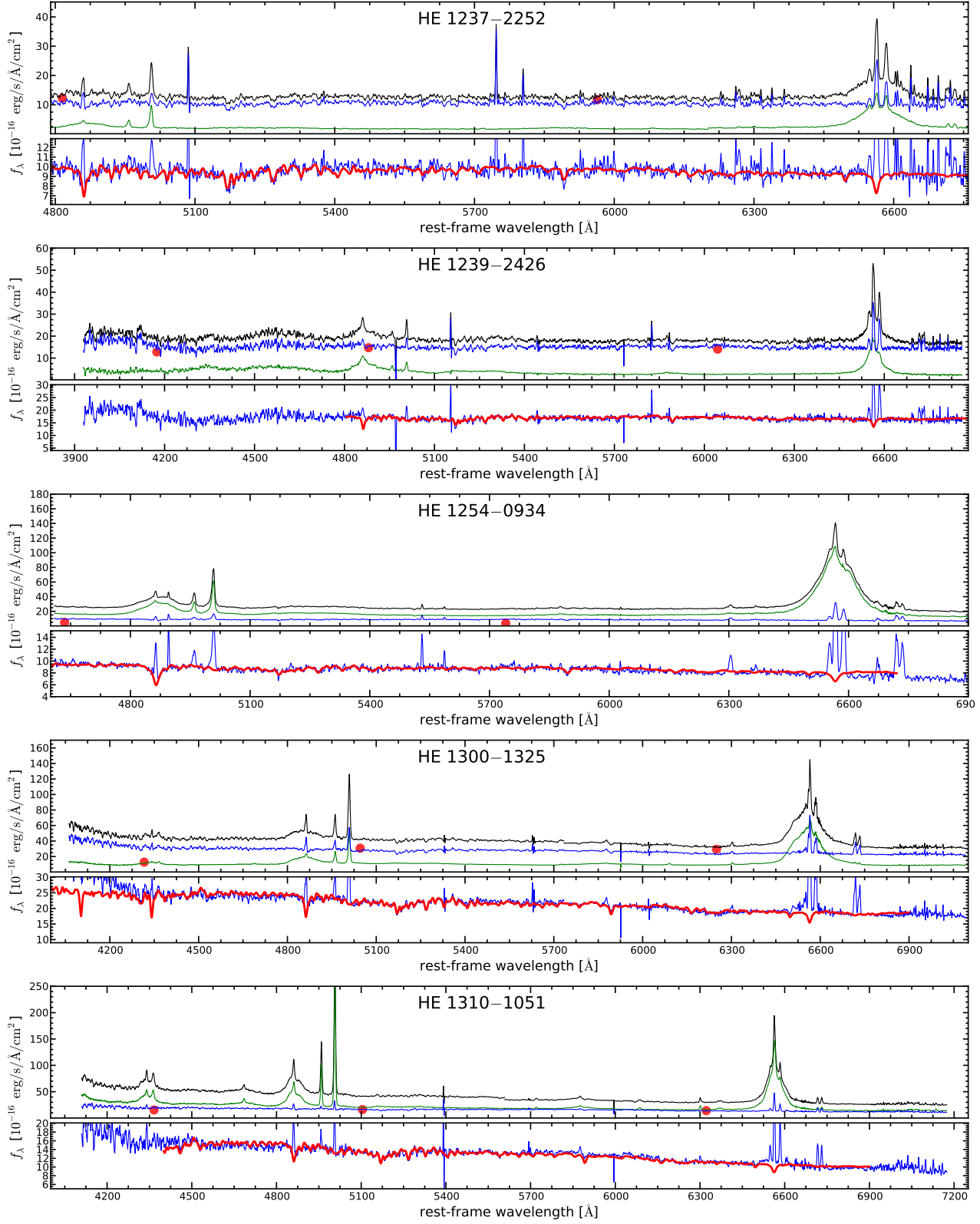
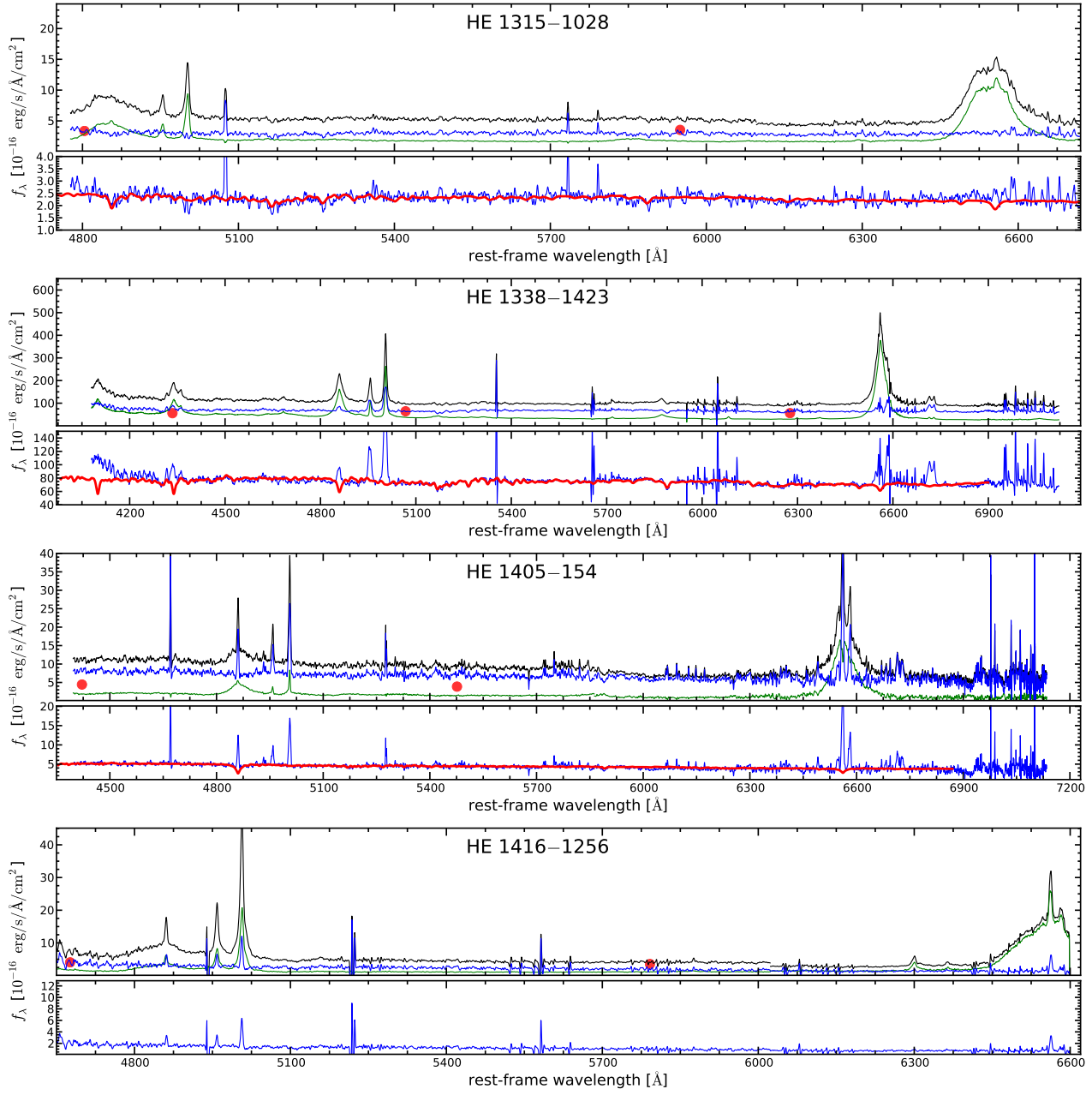


Figure B1 – continued

Figure B1 – *continued*